Research Square

Preprints are preliminary reports that have not undergone peer review.
They should not be considered conclusive, used to inform clinical practice,
or referenced by the media as validated information.

Expertise shifts predictive motor control from execution to error-corrective dynamics

Pavel Filip

pavel.filip@pm.me

Charles University, General University Hospital

Lenka Marková

Kantonsspital St. Gallen

Cecile Gallea

Institut du Cerveau–Paris Brain Institute–ICM, Inserm, CNRS, Sorbonne Université

Stéphane Lehéricy

Institut du Cerveau–Paris Brain Institute–ICM, Inserm, CNRS, Sorbonne Université

Ovidiu V. Lungu

University of Montreal

Shalom Michaeli

University of Minnesota

Silvia Mangia

University of Minnesota

Viktor Weiss

Masaryk University and St. Anne's Teaching Hospital

Martin Bareš

Masaryk University and St. Anne's Teaching Hospital

Lubomír Vojtíšek

Central European Institute of Technology, Masaryk University

Research Article

Keywords: motor learning; predictive control; error correction; functional MRI; network reorganisation; quantitative MRI; microstructural plasticity

Posted Date: June 25th, 2026

DOI: https://doi.org/10.21203/rs.3.rs-9996809/v1

License: This work is licensed under a Creative Commons Attribution 4.0 International License.
Read Full License

Additional Declarations: No competing interests reported.

Version of Record: A version of this preprint was published at The Cerebellum on November 4th, 2026.
See the published version at https://doi.org/10.1007/s12311-026-02100-4.

Expertise shifts predictive motor control from execution to error-corrective dynamics

Pavel Filip[1,2,3]*, Lenka Marková[4], Cecile Gallea[5], Stéphane Lehéricy[5], Ovidiu V. Lungu[6], Shalom Michaeli[3], Silvia Mangia[3], Viktor Weiss[7], Martin Bareš[7], Lubomír Vojtíšek[8]

[1] *Department of Neurology, Charles University, First Faculty of Medicine and General University Hospital, Prague, Czech Republic*
[2] *Department of Cybernetics, Czech Technical University in Prague, Prague, Czech Republic*
[3] *Center for Magnetic Resonance Research (CMRR), University of Minnesota, Minneapolis, MN, USA*
[4] *Canton Hospital St.Gallen Clinic for Anaesthesiology, Intensive Care, Rescue and Pain Medicine*
[5] *Institut du Cerveau–Paris Brain Institute–ICM, Inserm, CNRS, Sorbonne Université, Paris 75651, France*
[6] *Department of Psychiatry and Addictology, University of Montreal, Montreal*
[7] *First Department of Neurology, Faculty of Medicine, Masaryk University and St. Anne's Teaching Hospital, Brno, Czech Republic*
[8] *Central European Institute of Technology, Masaryk University, Brno, Czech Republic*

* Corresponding author: Pavel Filip
email: pavel.filip@pm.me

Short running title: Optimisation of predictive motor control

Keywords: motor learning; predictive control; error correction; functional MRI; network reorganisation; quantitative MRI; microstructural plasticity

Wordcount: 4,816
Number of tables: 1
Number of figures: 4

Abbreviations
AP – anterior–posterior; **AR** – autoregressive (model); **ARAS** – ascending reticular activating system; **ATAG** – atlas of the basal ganglia; **BOLD** – blood-oxygen-level-dependent; **CIFTI** – Connectivity Informatics Technology Initiative; **DWI** – diffusion-weighted imaging; **DVARS** – temporal derivative of timecourses root mean square variance; **ESS** – effective sample size; **FD_{95}** – 95th percentile of framewise displacement; **fMRI** – functional magnetic resonance imaging; **FA** — Flip angle; **GLM** – general linear model; **GM** – grey matter; **GRAPPA** — Generalized Autocalibrating Partial Parallel Acquisition; **HCP** – Human Connectome Project; **HRF** – haemodynamic response function; **ICA** – independent component analysis; **INLA** – integrated nested Laplace approximations; **iFOD2** – second-order integration over fibre orientation distributions; **MB** — Multiband; **MNI** – Montreal Neurological Institute; **MPRAGE** — Magnetization Prepared Rapid Acquisition Gradient Echoes; **MRI** — Magnetic resonance imaging; **NDI** – neurite density index; **NODDI** – neurite orientation dispersion and density imaging; **NUTS** – No-U-Turn Sampler; **ODF** – orientation distribution function; **ODI** – orientation dispersion index; **PA** – posterior–anterior; **PALM** – permutation analysis of linear models; **QC** – quality control; **$\widehat{R}$** — Gelman–Rubin convergence statistic; **SIFT2** – spherical-deconvolution informed filtering of tractograms 2; **SPACE** — Sampling Perfection with Application-optimised Contrasts using different flip angle Evolutions; **SPM** – Statistical Parametric Mapping; **TE** — Echo time; **TI** — Inversion time; **TR** — Repetition time; **tSNR** –

temporal signal-to-noise ratio; **$T_1\rho$** – adiabatic longitudinal relaxation in the rotating frame; **WAIC** – Watanabe–Akaike information criterion.

Funding statement: This study was supported by General University Hospital in Prague (MH CZ-DRO-VFN64165). P.F. was also supported by Brain Dynamics (grant number CZ.02.01.01/00/22_008/0004643).

Conflicts of interest: There are no potential conflicts of interests and/or financial relationships associated with this paper.

Data and code availability: Fully pre-processed parcellated MRI output (timeseries, NDI, ODI, $T_1\rho$), demographical information, behavioural performance, analytic outputs and supporting data values for presented figures are available as Supplementary Dataset. De-identified raw MRI data will be provided based on qualified academic request to the corresponding author.

Authors' contributions:
Conceptualisation: PF, LM, LV, SMi, SMa, MB
Data Curation: PF, LV
Formal analysis: PF
Funding acquisition: PF, LV
Investigation: LM, LV
Methodology: PF, CG, SL, OL, MB, VW, LV
Software: PF
Visualization: PF
Writing - original: PF
Writing – review & editing: PF, LM, CG, SL, OL, SMi, SMa, VW, MB, LV

Ethics approval: The study protocol was approved by the Ethics committee of the St. Anne's Teaching Hospital, Brno, Czech Republic (approval code 38V/2018).

Consent to participate: Each subject provided a written informed consent in accordance with the Declaration of Helsinki

Acknowledgements: The authors wish to express their sincere gratitude to the volunteers participating in the study. The authors also acknowledge the core facility MAFIL supported by MEYS CR (LM2023050 Czech-BioImaging), part of the Euro-BioImaging (www.eurobioimaging.eu) ALM and Multimodal Imaging Node (Brno, CZ).
In accordance with WAME guidelines, we acknowledge the utilisation of ChatGPT (OpenAI, GPT-5.2) for secondary word-processing assistance (grammar/stylistics evaluation and enhancement of text flow).

Abstract

Skilled motor behaviour relies on complex predictive control and error processing. Despite its indispensable position in our everyday lives, neurobiological mechanisms of motor skill acquisition remain poorly understood. The presented study evaluates the functional dynamics and microstructural substrate of expertise-related reorganisation in predictive timing circuits using multimodal functional and quantitative magnetic resonance imaging (MRI) data.

Forty-one baseball/softball players, representing a natural model of optimised motor timing programs, were compared against forty-six non-athletic controls using a structural connectome-informed hierarchical Bayesian framework jointly modelling task-based functional MRI dynamics of feedforward predictive control and error-driven modulation. The associated expertise-driven tissue reorganisation was then characterised using neurite orientation dispersion and density imaging and adiabatic $T_1\rho$ mapping.

In non-athletic controls, predictive control was found to engage a distributed cortico-subcortical sensorimotor, visuospatial, attentional and frontoparietal loops, while higher-order associative systems were relatively down-regulated. However, quantitative deviation from the task optimum was associated with progressive down-modulation of this predictive network. Expertise was characterised by higher behavioural performance but also by attenuated prediction-related functional engagement alongside enhanced error-related modulation. Furthermore, neurite density and orientation dispersion indices were higher in experts across distributed cortical networks, while the cerebellum exhibited a divergent profile characterised by higher neurite density, lower orientation dispersion and faster $T_1\rho$ relaxation.

These findings indicate that expertise involves a transition towards more efficient neural dynamics within an established architecture with coordinated rebalancing of fibre coherence, neurite compartment contribution and macromolecular environment, allowing for the reallocation of processing resources from task execution towards the management of unexpected information.

Introduction

Motor program optimisation stands at the core of our daily experience, enabling rapid, reliable and precise behaviour with minimal conscious supervision. It engages a distributed network system encompassing the cerebellum, basal ganglia, motor cortex and several brainstem structures (Baladron et al. 2023). Despite its central role, the mechanisms of adaptive motor regulation underlying motor skill acquisition and their optimisation to reduce the reliance on cognitive control, with its inherently limited capacity, remain poorly understood.

A classical perspective, rooted in early behaviourist and model-free reinforcement-learning concepts (Davison and Nevin 1999), ascribes adaptive behaviour to stimulus-response policies which are gradually strengthened via reward-based reinforcement (Botvinick et al. 2009). Nonetheless, converging theoretical and empirical work increasingly supports the view of brain architecture and both motor and non-motor programs as fundamentally predictive in nature (Clark 2013; Pezzulo et al. 2022). Organisms are conceptualised as self-regulating, goal-driven systems with internally specified reference states rather than passive stimulus-response automatons (Friston 2010; Pezzulo et al. 2015). Frameworks like good regulator theorem (Conant and Ashby 1970) and perceptual control theory (Powers 1973) then formalise behaviour as active re-alignment between internal models and their generated predictions with sensory observations actively sampled from the environment, utilising nested error-correction loops spanning several temporal and spatial scales. Indeed, several theoretical concepts propose central function of the neocortex in the generation of predictions about future state of both the external environment and internal conditions (Bar 2009), driving neural computations underlying perception and action across multiple domains (Korka et al. 2022; Den Ouden et al. 2012; Dercksen et al. 2024; Barron et al. 2020). These higher-order processes across distributed cortico-subcortical networks are then complemented by faster, high-fidelity predictive control at short time scales within the cerebellum (Baladron et al. 2023).

This framework indicates a complex, fluid processing environment driving skilled behaviour and predictive control optimisation. During the early phases of skill acquisition, ongoing deliberative feedback is an integral part of action selection with frequent corrective updates to achieve internal goals. Learning-associated performance improvement will then inherently require delicate re-balancing of increasing accuracy of internal prediction and selective higher-level corrections of detected errors. However, analytical separation of these conceptual counterparts using available measurement methods is non-trivial. Task functional MRI (fMRI) provides a neurobiologically plausible, yet indirect window into internal model use. Paradigms focusing specifically on predictive timing (Filip et al. 2017; 2016) offer a viable opportunity to dissociate prediction-related neural programs from motor execution *per se*. Participants generate and update estimates of future state, engaging cortico-cerebellar and cortico-basal ganglia circuits, which allows for the observation of the complex prediction-related sensorimotor internal models even within extensive in-scanner movement limitations.

The presented study utilises this paradigm in a population where long-term, in-depth experience with predictive control is a core feature. Baseballers are a natural model of expertise-driven program optimisation and have been previously shown to outperform non-athletic controls in movement-based prediction (Marková et al. 2020). In the current mechanistic extension of our previous efforts, the overarching aim was to dissociate the effect of optimisation into its two major presumed components – tonic control processes responsible for predictive task execution and transient error-driven updates mitigating deviations from an internal optimum. We hypothesised that predictive control optimisation would be associated not only with higher effectiveness – more accurate internal predictions with lower need for deviation correction– but also with higher efficiency – expressed as hyper-optimisation of predictive motor networks where greater behavioural performance is achieved with smaller fMRI signature. Furthermore, we tested whether program optimisation is also associated with underlying tissue

reconfiguration utilising indirect microstructural proxies of dendritic complexity and macromolecular content derived from neurite orientation dispersion and density imaging (NODDI) (Kamiya et al. 2020) and adiabatic longitudinal relaxation (Michaeli et al. 2006), respectively.

Methods

43 baseball/softball players (hereinafter experts) (12 females – softball players, 31 males – baseball players; median age 24, range 17-37) and 46 non-athletic controls (15 females, median age 24.5 [18–39]) were enrolled into this study. All experts were selected from the Czech Baseball National Team or high-level domestic league, with at least 10 years of competitive experience. All participants were right-handed according to the Edinburgh Handedness Inventory and reported no history of neurological and/or psychiatric complaints or standard MRI contraindications. Every participant provided their written consent in accordance with the Declaration of Helsinki. The study protocol was approved by the ethics committee of the Ethics Committee of the University Hospital of St. Anne, Czech Republic (approval code 38V/2018).

Experimental Task

Participants performed a previously published motor timing task (Filip et al. 2017). In the main time-estimation condition ("shooting"), participants pressed a button to launch a vertically moving projectile to intercept a circular target moving from the left side of the screen at one of three possible speeds (Figure 1A). The deliberately low velocity of the projectile required anticipatory timing – button had to be pressed before the target reached the fixed interception zone in the upper right corner, to account for the time needed by the projectile to also reach the interception area. The diagonal angles of the target trajectory were selected randomly to limit learning. A control condition ("cross") matched visual input characteristics and motor output of the main condition but lacked the predictive timing aspect since button press was required when the target entered a zone explicitly marked with a cross (Figure 1B). Visual feedback indicated hit or miss after each trial in the form of a green or red fixation point, respectively, presented in the centre of the screen for about 5 seconds (with random jitter of ±1 second) after each trial. Trials were organised into blocks of 10 shooting trials followed by 10 cross trials, repeated three times per session, with target speed randomised to provide 10 high/medium/low-speed trials per condition (shooting/cross). Participants completed a brief training session during the acquisition of the preceding structural scans.

MRI Data Acquisition and Processing

MRI data was acquired using a 3 Tesla Siemens MAGNETOM Prisma with 64-channel head/neck coil at the Central European Institute of Technology in Brno, Czech Republic, with the following protocol covering the whole brain including the brainstem and cerebellum (except $T_1\rho$, see below):

- T_1-weighted (MPRAGE): isotropic 0.8 mm^3; repetition time (TR) / echo time (TE) / inversion time (TI) = 2,300/2.28/1,000 ms; flip angle (FA) 8°; GRAPPA 3.
- T_2-weighted (SPACE): isotropic 0.8 mm^3; TR/TE = 3,200/409 ms; GRAPPA 2.
- Diffusion-Weighted Imaging (DWI): isotropic 1.5 mm^3; TR/TE = 3,230/89.2 ms, effective echo spacing 0.69 ms; multiband (MB) acceleration factor 4; two non-zero shells b = 1,500/3,000 $s.mm^{-2}$, 93 directions, 7 interleaved b0 volumes; acquired twice with reversed phase-encoding (antero-posterior [AP], and postero-anterior [PA]) (Harms et al. 2018).
- fMRI (blood-oxygenation-level–dependent (BOLD) gradient-recalled echo echo-planar imaging): 3 sessions, isotropic 2.0 mm^3; TR/TE = 820/35.2 ms; FA 45°; MB 4, PA phase encoding; 590 volumes per session; Spin-echo fieldmaps (AP/PA) were acquired for distortion correction.
- Adiabatic $T_1\rho$: acquired only over a slab covering the cerebellum and basal ganglia; in-plane resolution 1.0 × 1.0 mm^2, slice thickness 3 mm, 23 slices in total; TR/TE = 2,000/2.33 ms; GRAPPA 3;

AFP HS4 pulses (R = 10, duration 6 ms; 0–16 pulses [0/4/8/12/16; 0–96 ms] phase-cycled by MLEV-4; bandwidth 1.3 kHz; $\omega_1 max/(2\pi)$ = 800 Hz) (Garwood and DelaBarre 2001; Levitt et al. 1982).

The processing pipeline was based on the Human Connectome Project (HCP) minimal preprocessing pipeline, including the optional correction of gradient non-linearity and susceptibility-related B_0-field distortions (Glasser et al. 2013) and the subsequent ICA+FIX denoising of fMRI data (Smith et al. 2013). DWI data processing implemented upstream denoising based on random matrix theory with Marchenko-Pastur distribution modelling (Veraart et al. 2016) utilising the optimised patch-based singular value shrinkage method (Cordero-Grande et al. 2019), the removal of Gibbs ringing artefacts via local subvoxel shifts (Kellner et al. 2016), followed by the HCP minimal preprocessing pipeline architecture with mitigation of eddy-current distortions extended by slice-to-volume motion correction (Andersson et al. 2017), outlier replacement (Andersson et al. 2016) and susceptibility-by-movement interaction correction (Andersson et al. 2018). A three-tissue response function was estimated and used for multi-shell multi-tissue constrained spherical deconvolution to derive fibre orientation distributions (Jeurissen et al. 2014), followed by multi-tissue log-domain intensity normalisation. Anatomically constrained probabilistic tractography (FreeSurfer-informed) was performed using iFOD2 with dynamic seeding to generate 10 million streamlines (Smith et al. 2012), which were subsequently reweighted using SIFT2 to obtain quantitative connectivity estimates (Smith et al. 2015).

Microstructural parameter estimation fitted the NODDI-Bingham model to DWI data using Bayesian inference framework with Markov chain Monte Carlo sampling (Tariq et al. 2016), with 5,000 burn-in iterations followed by 25,000 iterations with thinning by a factor of 25, yielding voxel-wise neurite density index (NDI) and orientation dispersion index (ODI). NDI and ODI maps were then sampled onto subject-specific mid-thickness cortical surface using cortical-normal interpolation with grey matter weighting to minimise partial volume effects. Mapping of $T_1\rho$ relaxation time constant was preceded by 3D rigid-body realignment of all volumes to the first scan (mutual information cost function with trilinear interpolation, with subsequent sinc interpolation refinement). Voxel-wise signal evolution was modelled using a two-parameter mono-exponential decay model to estimate the equilibrium signal intensity and the relaxation time constants with non-linear optimisation (Nelder-Mead simplex).

All processing outputs implemented a hybrid parcellation scheme combining HCP multimodal atlas (180 parcels per individually reconstructed hemispheric cortical surface) (Glasser et al. 2016) and additional standard-space atlases: structural cerebellar (Diedrichsen et al. 2009), Oxford-GSK-Imanova striatal (Tziortzi et al. 2014), Oxford thalamic connectivity (Behrens et al. 2003), hypothalamic (Spindler et al. 2020), ARAS (Edlow et al. 2012), ATAG (Keuken et al. 2017) and hippocampal atlas (Winterburn et al. 2013), collectively covering full extent of subcortical grey matter. Subcortical atlas masks were warped from the standard to individual T_1-weighted space and rigidly aligned to DWI/$T_1\rho$ mapping space in a single resampling step with trilinear interpolation. Regional values were calculated as parcel-level probability-weighted means. For fMRI data, HCP CIFTI cortical and standard-space output was utilised for parcellated timeseries extraction. For $T_1\rho$, only subcortical grey-matter parcels were considered due to limited acquisition coverage.

Quality Control (QC)

Two participants (both in the expert group) failed to complete the task fMRI acquisition and were excluded from further analysis. Moreover, $T_1\rho$ acquisition was not available for one further participant (expert) and, as a secondary metric, was imputed parcel-wise using hot-deck imputation: a donor participant was selected from the same group based on nearest-neighbour similarity in z-scored subcortical NDI and ODI profiles.

Subject-wise QC was performed in three tiers:

- Tier 1 (motion; hard criterion): sessions with pronounced motion spikes (95th-percentile framewise displacement [FD_{95}] > ½ voxel: 1 mm for fMRI; 0.75 mm for DWI) were excluded.
- Tier 2 (multivariate stability): robust Mahalanobis distance based on the orthogonalised Gnanadesikan–Kettenring scatter matrix was calculated per session/modality from five stability metrics and flagged at $\chi^2_{(5;\,0.999)} = 20.52$. For fMRI, these were FD_{95}, 95th percentile DVARS on residualised parcel timeseries, mean high-frequency power fraction (0.20–0.45 Hz relative to 0.01–0.45 Hz), 95th-percentile global-signal derivative, and mean fraction of extreme amplitudes (|robust z|>5). For DWI, these were FD_{95}, eddy slice-outlier fraction, reduced χ^2 of the diffusion tensor fit, SIFT2 weight dispersion, and connectome edge density.
- Tier 3 (biological plausibility): sessions flagged in Tier 2 were excluded only if arbitrarily selected connectivity-based metrics not considered in the main analyses (homotopic symmetry and global connectivity) showed substantial within-cohort deviation (|robust z|>5 in either metric).

Sessions failing Tier 1, or both Tier 2 and Tier 3, were to be excluded; only participants passing QC for DWI and all three task fMRI sessions were retained. These criteria did not flag any further subjects for exclusion. Ergo, the final analysis comprised 41 experts (group summary characteristics unchanged: 12 females, age 24 [17–37]) and 46 controls (15 females, age 24.5 [18–39]).

Parcel-wise QC was based on five technical fMRI measures (temporal signal-to-noise ratio, motion coupling, high-frequency contamination, spike rate, global signal leverage) averaged over the three task fMRI sessions and five technical DWI metrics (diffusion model misfit, thermal noise variance, streamline reduction ratio, absent-edge fraction, streamline weight entropy). Robust Mahalanobis distances were computed within subjects separately for cortical and subcortical parcels due to inherent hardware-related differences in signal characteristics and aggregated per parcel across subjects using median. 30 parcels exceeding $D^2 > \chi^2_{(10;\,0.999)} = 29.59$ (generally located in artefact-prone areas, see Supplementary figure 1) were excluded from all the following analyses.

Activation Analysis

At the first level, task-related BOLD responses were modelled using event-related general linear model (GLM), with trial onsets set to the appearance of the target on the left side of the screen and durations to response times (button press). Condition- and speed-specific differences in the haemodynamic response were captured by partitioning into six condition cells distinguishing the main (shooting) and control (cross) tasks at each of the three target speeds. Trial-wise performance was quantified using timing error defined as the signed difference between the response time and calculated trial-specific optimum. Since temporal tolerance of successful hit varied with target speed, timing error was normalised within each speed level by robust estimate of its dispersion across trials. This speed-invariant measure of trial performance was again modelled separately for each condition and speed type (six regressors). Lastly, given the 10-trial block structure, two condition-specific nuisance regressors were constructed to capture block-wise variation, modelling block repetition separately for the shooting and cross task blocks (mean-centred within each session). All task and covariate regressors were subsequently convolved with the SPM canonical haemodynamic response function (30 s kernel) and sampled at fMRI acquisition times to form a volume-level design matrix. The resulting design matrices exhibited low collinearity, with variance inflation factors for all regressors below 2.

Further subject-level processing of parcellated fMRI timeseries implemented spatial Bayesian general linear modelling approach using integrated nested Laplacian approximations (INLA) (Mejia et al. 2020) instead of standard mass-univariate analyses. This approach enabled joint estimation of task effects with explicit modelling of inter-parcel spatial dependence derived from subject-specific structural connectomes, providing higher robustness to noise and full posterior uncertainty quantification for downstream group analyses. Following the removal of nuisance variance attributable to head motion (six rigid-body parameters with temporal derivatives) and low-order drifts (linear and quadratic trends) from both the

task regressors and parcellated fMRI signal, the residualised timeseries were temporally prewhitened using AR(p) model fitted to GLM residuals using Yule-Walker estimation (Mejia et al. 2020). A single global model order was selected empirically by session-wise comparison of candidate orders (p = 1–16) using Ljung-Box whiteness tests (lag 24). The smallest order meeting a pre-specified conservative QC target (≥90% of sessions with ≥95% parcels passing) was selected, yielding AR(4) (see Supplementary figure 2). Subsequently, session-wise task-related regression coefficients were estimated within a single spatial Bayesian GLM utilising R-INLA (Lindgren and Rue 2015), where contrary to the reference pipeline (Mejia et al. 2020), spatial dependence of parcel-wise effects was modelled using a Laplacian precision matrix derived from subject-specific structural connectome rather than a purely distance-driven mesh smoothness prior. This extension explicitly allowed for biologically informed long-range dependencies (e.g. cerebello-cortical coupling), directly addressing a limitation noted in the reference pipeline. All INLA fits converged without numerical failures, marginal likelihood was finite for all models (median -3.97×10^5), and global fit metrics were stable (median Watanabe–Akaike information criterion (WAIC) 7.25×10^5).

Group-level Analysis

Task-related activation analysis was based on a second-level Bayesian hierarchical model implemented in Stan (see Supplementary Methods for full description). First-level INLA regression coefficients were collapsed into the main contrasts of interest: shooting–cross difference across all speed levels, linear speed scaling of the shooting–cross difference, and two analogous contrasts for the timing-error modulation. Contrast uncertainty was propagated from the full posterior covariance tensor of the first-level INLA coefficients to retain correlations between first-level regressors. The four main contrasts were modelled jointly within a single hierarchical model using clique-based regularisation – parcels were grouped into higher-order anatomical territories and modelled via clique pooling with parcel-level deviations (see Supplementary Table 1). The primary effects of interest for the four contrasts were: (i) control-group mean effect at the session-centred exposure level, and (ii) expert–control difference. The model further considered: (iii) linear session trend, (iv) group-by-session interaction, and (v) age and sex. Main effects of interest included parcel-specific deviation term, whereas nuisance terms were estimated at clique-level only (to improve model stability). Regression parameters were assigned weakly informative Gaussian priors; hierarchical scale parameters and the additional residual scale (variance beyond propagated first-level uncertainty) received half-normal priors. Posterior inference used Hamiltonian Monte Carlo (4 chains, 750 warm-up iterations and 750 sampling iterations per chain, target acceptance probability 0.90, maximum NUTS tree depth 12), yielding 3,000 posterior draws.

Microstructural metrics (NDI, ODI and $T_1\rho$) were z-scored per parcel across subjects and modelled jointly within the same hierarchical clique-regularised structure as above (absent cortical parcels for $T_1\rho$ handled via an observation mask), with equivalent sampling settings and priors. The main effect of interest was the expert-control group difference.

Both second-level Bayesian models exhibited good convergence and sampling behaviour ($\hat{R} \leq 1.01$, high bulk/tail ESS, and no divergent transitions or tree-depth saturations; Supplementary Table 2).

Lastly, supplementary robustness analyses were performed to validate activation patterns detectable using the proposed Bayesian pipeline against previously published legacy methods (Filip et al. 2017) and to address potential concern of the hierarchical models overly favouring clique-level structure using an alternative model with explicitly prioritised parcel-level effects (see Supplementary Methods and Supplementary Figure 3).

Results

Behavioural analysis corroborated previously published results (Marková et al. 2020). Experts exhibited higher accuracy in the main shooting task (median hit ratio [10^{th}–90^{th} percentile] of 0.68 [0.52–0.77]) than controls (0.53 [0.44–0.68]), largely overlapping performance in the control cross task (experts 0.86 [0.70–0.90] and controls 0.81 [0.72–0.91]) (see Figure 1C) and similar difficulty (speed) scaling characteristics (see Figure 1D).

Task-Related Activation Analysis

In Controls, **motor prediction** (shooting > cross) was associated with robust positive effects across the sensorimotor network, dorsal attention network, visual regions and frontoparietal control networks, encompassing also their subcortical and cerebellar elements (see Figure 2, Table 1). Systematic negative components were detected within mostly midline default-mode network hubs and episodic memory related systems, such as hippocampus.

By contrast**, error modulation** in the control cohort was characterised by predominantly negative effects within the same sensorimotor, attention- and control-related networks shown to be positively engaged by the motor prediction contrast. Furthermore, regions negatively modulated during motor prediction, such as mesiotemporal cortex and posterior cingulate, exhibited a reversal of their prediction-associated suppression.

Group comparison over the motor prediction contrast indicated narrower dynamic range between task-positive and task-negative components in experts, as evidenced by their attenuated responses within main cortico-subcortical sensorimotor and dorsal parietal networks. On the other hand, experts showed relatively higher response magnitude to increasing deviation from the task optimum within large-scale frontoparietal and visuospatial networks as compared with controls.

Difficulty (speed) scaling analysis revealed predominantly positive control-group mean effect over frontotemporal and visuospatial networks, with additional involvement of limbic system components (see Figure 3, Supplementary Table 3). Other subcortical structures showed posterior credible intervals largely centred around zero. Response to error with rising speed was negative, with spatial distribution similar to the speed-independent error-modulation effect. When compared to controls, experts exhibited attenuated speed-dependent motor prediction response, mostly in the occipito-temporal cortices, but also in hippocampal region. In contrast, speed scaling of error modulation was higher in experts in the mesiofrontal and secondary visual cortex.

Microstructural Group Comparison

Experts showed modestly, but spatially consistent higher NDI and ODI relative to controls within dorsal attention, sensorimotor, and frontoparietal control networks, while differences in NDI over midline default-mode network hubs and frontal cortico-subcortical loops were detected only in NDI. On the other hand, cerebellum exhibited a mixed microstructural profile, with higher NDI in experts dominantly in lobules VI and VIII, co-occurring with oppositely directed ODI and $T_1\rho$ effects, mostly over cerebellar crura and lobule VIII. Lastly, limbic system showed slower $T_1\rho$ relaxation and lower ODI in experts, whereas NDI credible intervals were effectively zero-centred.

Discussion

The presented results indicate that intensive motor training is associated with a reconfiguration of large-scale networks – both their dynamical patterns and microstructural foundations. Higher behavioural

performance in experts was associated with reduced reliance on primary task-positive sensorimotor and visuospatial network activation and enhanced error processing response within overlapping task-relevant structures. This framework aligns well with the established principle of cerebral networks becoming more efficient at generating accurate neural outputs with practice (Picard et al. 2013), redistributing available processing capacity towards deviation management and integrative control. Crucially, resolving these distributed patterns of relatively modest magnitude required a more holistic analytical approach integrating structural connectome and hierarchical modelling framework.

Shift from Cerebellar Dominance to Distributed Predictive Control Networks

In our earlier studies employing the same predictive timing paradigm (Filip et al. 2016; 2017; 2019; Bares et al. 2011), cerebellum emerged as the dominant neural correlate of motor prediction, supporting its role as the principal driver within short-scale predictive timing processes. The presented structural connectome-informed hierarchical analysis reveals a more distributed architecture encompassing large-scale cortico-subcortical systems. Even general population without long-term motor training (see Figure 2 – Control-group mean effect) processes temporal prediction over sensorimotor, visuospatial, attentional and frontoparietal control systems together with striatal, thalamic and cerebellar loops, while disengaging default-mode network hubs. Predictive control thus emerges as an inherently network-based algorithm, shifting the cerebellum to the position which, while prominent, remains deeply embedded within a larger hierarchical architecture. This concept is well aligned with the emerging view of motor learning, process optimisation and general cerebral processing patterns as an interplay between distributed networks with hierarchical organisation and information transfer, rather than the function of a single dominant node (Caligiore et al. 2019a). Interestingly, the quantitative deviation from the task optimum was associated with down-modulation of this predictive network, indicating weaker or less stable engagement of internal models with larger prediction errors rather than the recruitment of error-driven corrective processes described previously (Den Ouden et al. 2012).

Expertise-Driven Shift from Predictive to Error-Corrective Dynamics

One of the main findings of this study – reduction in prediction-related functional signal with expertise combined with superior behavioural performance – points to a transition towards a more efficient neural dynamics within an established architecture rather than the emergence of qualitatively distinct networks. Performance has become less effortful over repeated trials in experts as circuitry shifted from dispersed neural regions to highly optimised networks mediating more efficient processing. These findings thus extend previous reports of decreased functional activity in highly skilled musicians, generally limited to motor areas in simple motor tasks (Hund-Georgiadis and von Cramon 1999; Jäncke et al. 2000; Meister et al. 2005), to reverberations across large-scale networks encompassing dorsal parietal and cortico-subcortical sensorimotor loops (see Figure 2 – Expert–Control Difference).

This pattern was further supported by the difficulty-dependent effects (see Figure 3). Regions exhibiting relative down-regulation in the main task in controls, including temporal, limbic and prefrontal systems, were progressively engaged with rising task demands, possibly indicating adaptive dynamic recruitment of higher-order supervisory systems when feedforward prediction models were becoming insufficient. Importantly, this scaling effect was markedly attenuated in experts who responded to increasing uncertainty with stronger targeted engagement of these very regions during error processing.

However, our initial hypothesis of error signal minimisation with expertise-driven optimisation of internal prediction models and hence their presumed higher accuracy was not confirmed. Contrary to that, processing capacities were redistributed to a different regime – from dominantly predictive, feedforward to error-corrective mode, employing the reserves for the management of departures from the expected optimum (Tsay et al. 2022). Neurobiologically, this framework mirrors efficient coding concepts, where

brain reduces redundancy in neural signals within established pathways and reallocates processing resources to unexpected information (Młynarski and Tkačik 2022).

Given the distributed characteristics of both expertise-related effects, predictive timing program optimisation does not seem to be dominated by one process or one anatomical region, resonating with the concept of super-learning (Caligiore et al. 2019b; 2017). In contrast to more fragmented notions attributing cerebellar architecture to supervised learning (Raymond et al. 1996), basal ganglia to reinforcement learning (Doya 2000) and cortex to unsupervised learning (Matteucci et al. 2024), this view proposes the brain as a synergic, hierarchical integrative system being iteratively updated through feedback mechanisms and predictive error-based correction.

Expertise-Related Microstructural Remodelling of Predictive Networks

The microstructural profile associated with expertise revealed spatially coherent, but only modestly higher NDI and ODI over sensorimotor, frontoparietal control and dorsal attention networks (see Figure 4), in line with growing evidence of cortical microstructural remodelling accompanying skill acquisition (Lehmann et al. 2023; Tavor et al. 2013). Although NODDI is inherently ill-posed for fully resolving microstructural complexity of grey matter at the spatial resolution of available DWI protocols, converging evidence from various acquisition schemes, analytical approaches and biological models indicates dendritic architecture as a dominant contributor of cortical diffusion indices (Aggarwal et al. 2015; Budde and Annese 2013). While highly inferential in nature, higher NDI and ODI in experts may be seen as markers of increased dendritic arborisation complexity, reflecting experience-related reconfiguration as a putative backbone of optimised predictive networks. Indeed, learning-related plasticity has been shown to include selective pruning of dendritic spines and connection strengthening (Roo et al. 2008; Schifani et al. 2022).

Compared to this relatively uniform cortical pattern, the cerebellum exhibited substantial divergence in individual metrics – relatively higher NDI with lower ODI and $T_1\rho$, particularly within the cerebellar crura. This dissociation likely stems from its highly specialised architecture and processing patterns uniquely suited for algorithmic corrections and reconciliation of predicted sensorimotor consequences of planned actions with observed outcomes (Bareš et al. 2019). Massive parallelisation, highly regular microcircuitry, dense parallel fibre organisation and climbing fibre-driven synaptic plasticity not only allow for rapid update of internal models (Hull 2020; Tanaka et al. 2020), but may predispose the cerebellum to embrace selective increase of directional coherence within dominant fibre populations as a substrate of program fine-tuning. Concomitantly shorter $T_1\rho$ relaxation time points to enhanced interactions between water protons and the macromolecular environment (Michaeli et al. 2009; Davis et al. 1994; Fischer et al. 1998), compatible with the concept of experience-dependent synaptic remodelling and intracellular processes related with increased plasticity (Fu and Zuo 2011).

Limitations and Methodological Considerations

While the presented analytical framework enabled the detection of distributed effects of network optimisation and associated dynamical mode shifts that would not be accessible using conventional voxel-wise mass-univariate approaches, the cost reflected in computational and methodological complexity is substantial. High-resolution surface-based analysis using the HCP pipeline combined with probabilistic structural connectome reconstruction required extensive subject-level preprocessing, while hierarchical Bayesian model (see Supplementary Methods), integrating network-regularised spatial inference with fully generative multi-level modelling of interacting task components, extends beyond the scope of commonly employed neuroimaging packages.

This level of complexity represents both the major strength and the primary limitation of the presented study. Advanced parcellation clearly improved cortical effect localisation and helped preserve network organisation compared to standard-space atlas pipelines (see Supplementary Figure 3). Ultimately, subtle,

but coherent distributed effects became stable only under a unified generative model with proper propagation of uncertainty over analysis levels and across parcels, with inference constraints along biologically meaningful pathways derived from structural connectome replacing the standard, purely local spatial dependence assumptions. This concept contrasts with conventional, mass-univariate analyses which inherently fragment complex dynamics into independent tests.

Additionally, the cross-sectional design comparing experts and controls precludes causal inference about expertise-driven network reorganisation since pre-existing neurobiological predispositions may contribute non-negligibly both to microstructural and functional profiles. However, contrary to the conditions in North America, athletic selection pressure is likely substantially lower in the present regional context where baseball is not a dominant sport. Secondly, the generalisability of detected optimisation patterns to other predictive and fine-tuning processes remains to be fully established, although previous unimodal studies in different populations have reported isolated components consistent with present findings – both expertise-related attenuation of functional activity (Hund-Georgiadis and von Cramon 1999; Jäncke et al. 2000; Meister et al. 2005) and ODI increase (Lehmann et al. 2023). Finally, all MRI metrics are conceptually only indirect, model-dependent proxies of underlying biology. The BOLD signal reflects haemodynamic processes rather than true neural activity and may therefore be affected by group differences in vascular dynamics – an important consideration for the comparison of athletes and non-athletic controls. However, superior vascular fitness would be expected to produce higher rather than attenuated BOLD response in experts in the main motor prediction contrast, strengthening the proposed interpretation of more efficient network optimisation.

Conclusion

In summary, this multimodal synthesis presents the coordinated reorganisation of both functional and microstructural characteristics underlying optimisation of predictive mechanisms at network-wide levels. The expertise-driven shift from dominantly predictive to error-corrective mode, enabling reallocation of processing resources towards unexpected information, emerges as the hallmark of optimised hierarchical control. Furthermore, its combination with coordinated rebalancing of fibre coherence, neurite compartment contribution and macromolecular environment provides plausible microstructural foundations consistent with experience-driven plasticity supporting these dynamics. Future longitudinal studies investigating the joint development of functional optimisation, its underlying microstructural changes, as well as their coupling, will be essential to elucidate this concept.

Figures

Figure 1. Behavioural task design and group performance. (A) Schematic of the main "shooting" predictive timing task. A moving target (red ball) flew from the left side of the screen under random angles into the right upper corner to be intercepted by a projectile fired by the participant vertically from the right lower corner. Dashed arrows indicating trajectories for visualisation purposes were not present on the screen. (B) Schematic of the control "cross" condition, where participants responded when the ball reached the fixed cross positioned randomly over the second half of the target trajectory. (C) Main vs control task performance shown as split violin plots of proportional hit rate, aggregated per participant across sessions and speed levels. Shooting (red, left half) and Cross (blue, right half) shown separately for Experts and Controls. Solid horizontal lines indicate medians; dashed lines indicate quartiles. (D) Speed scaling of main task performance. Group-wise median hit rate across low/medium/high speed levels with shaded interquartile range. No inferential statistics provided, see (Marková et al. 2020) for detailed analyses. Full numerical results underlying the figures are provided in the Supplementary Dataset.

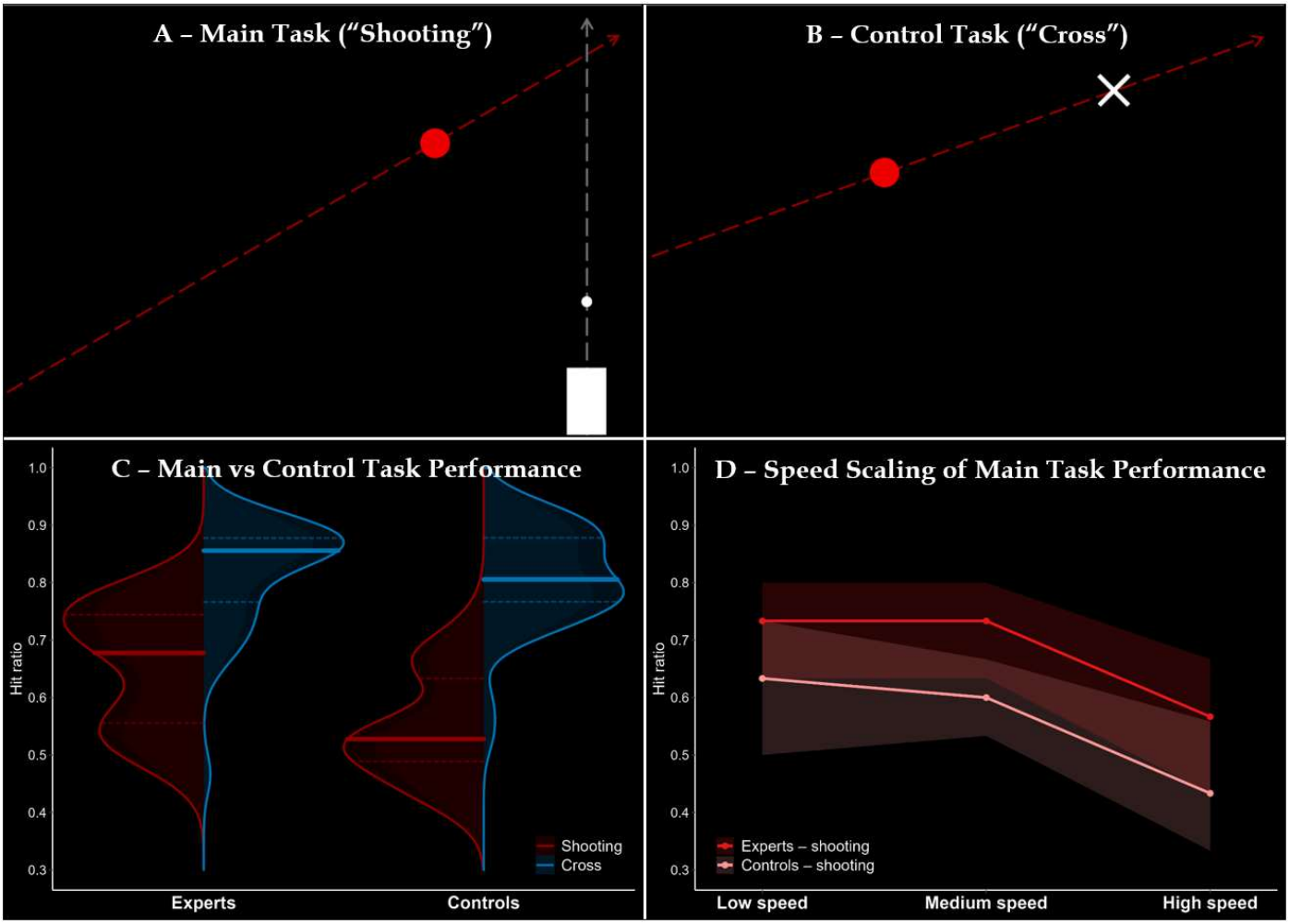


Figure 2: Results of second level task-related activation effects for motor prediction (shooting–cross) **and error modulation** (within the same contrast), separately for control-group mean effect and expert–control difference. Depicted as posterior medians (multiplied by 10^3 to improve colour scale legibility) thresholded at a posterior sign probability ≥0.95. Motor prediction shows positive effects within sensorimotor, dorsal attention, visual, and frontoparietal control networks with coincident negative components in default-mode and episodic memory–related systems; error modulation in controls exhibits negative effects within the task-positive networks. Expert-control differences are dominated by relatively lower motor-prediction effect magnitude in experts, but higher activation associated with error magnitude. Shown in combined cerebral surface reconstructions with subcortical standard space in 6 slices (z = 16, 2, -12, -26, -40, -54). Laterality follows radiological convention (the right side of the image corresponds to the right side of the brain). See Table 1 for more detailed statistical results and anatomical localisation. Full numerical results underlying the figures are provided in the Supplementary Dataset.

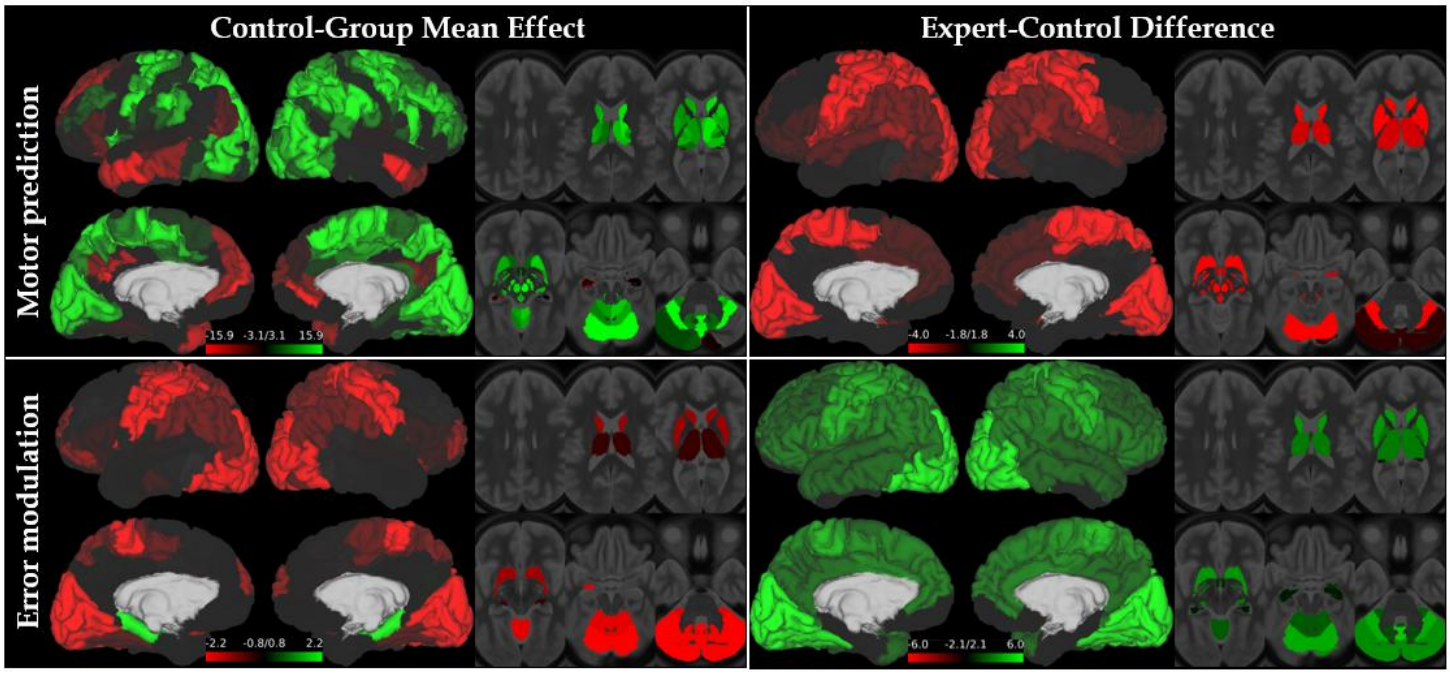


Figure 3: Results of second level task-related activation effects for difficulty (speed) **scaling of motor prediction** (shooting–cross) **and error modulation (**within the same contrast), separately for control-group mean effect and expert–control difference. Depicted as posterior medians (multiplied by 10^3 to improve colour scale legibility) thresholded at a posterior sign probability ≥0.95. Speed scaling of motor prediction is expressed mostly within frontotemporal, visuospatial networks and limbic structures, while in error-modulation, it shows largely negative effect in controls. Experts exhibited relatively lower extent of speed-dependent modulation of predictive timing in temporal and visual cortices, but relatively higher error-related responses with increasing speed mostly frontally. Shown in combined cerebral surface reconstructions with subcortical standard space in 6 slices (z = 16, 2, -12, -26, -40, -54). Laterality follows radiological convention (the right side of the image corresponds to the right side of the brain). See Supplementary Table 2 for more detailed statistical results and anatomical localisation. Full numerical results underlying the figures are provided in the Supplementary Dataset.

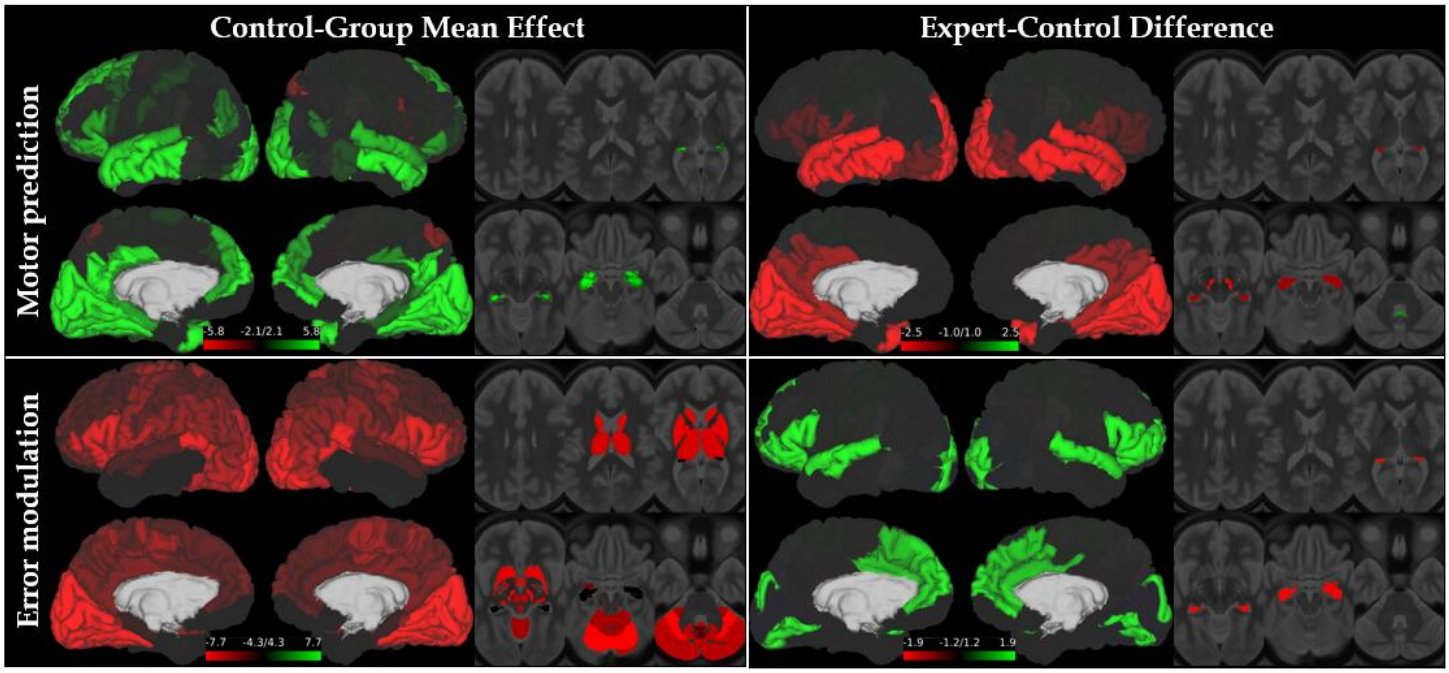
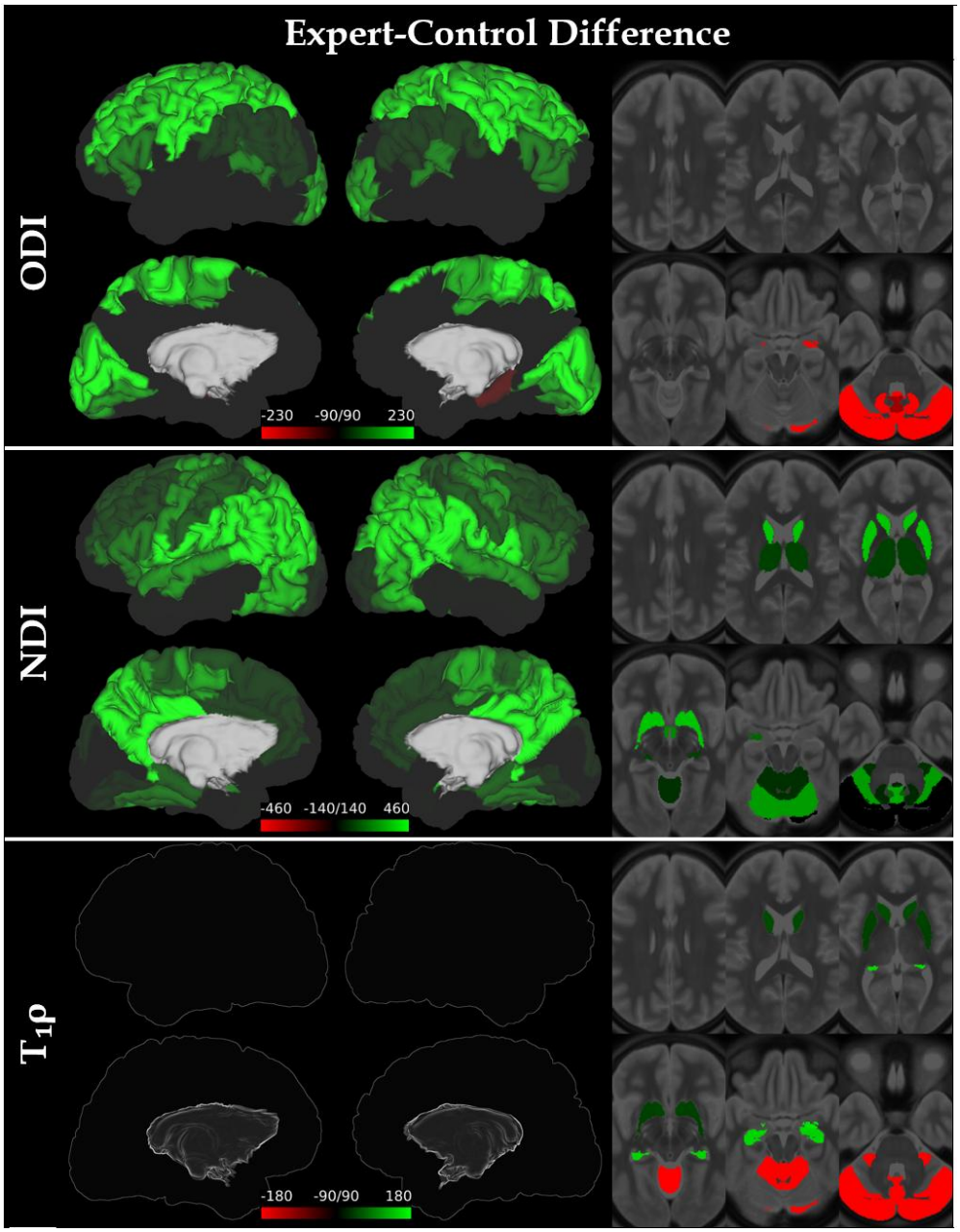


Figure 4: Inter-group comparison of microstructural metrics – Neurite Density Index (NDI), Orientation Dispersion Index (ODI) and adiabatic $T_1\rho$ relaxation constant (analysed only in subcortical structures due to the field of view utilised in the MRI acquisition). Depicted as posterior medians (multiplied by 10^3 to improve colour scale legibility) thresholded at a posterior sign probability ≥0.95. Experts showed relatively higher ODI and NDI over visual, dorsal attention, sensorimotor, and frontoparietal control networks, but exhibited a relatively mixed microstructural profile in the cerebellum. Shown in combined cerebral surface reconstructions with subcortical standard space in 6 slices (z = 16, 2, -12, -26, -40, -54). Laterality follows radiological convention (the right side of the image corresponds to the right side of the brain). See Supplementary Table 3 for more detailed statistical results and anatomical localisation. Full numerical results underlying the figures are provided in the Supplementary Dataset.



Tables

Table 1: Results of second level task-related activation effects for motor prediction (shooting–cross) **and error modulation (**within the same contrast). Corresponding spatial maps provided in the Figure 2. Reported over larger anatomical partitions (cliques, see also Supplementary Table 1) separately for control-group mean effect and expert–control difference. Values provided as posterior medians with 95% credible intervals (CrI) (multiplied by 10^3 for numerical clarity) and posterior probability that the effect has the reported sign (P(sign)). Arrows indicate effects whose 95% CrI excludes zero (↑ positive, ↓ negative); effects with CrI spanning zero shown in grey. The ordering of cliques follows anatomical hierarchies across cortical, subcortical and cerebellar systems. Full numerical parcellated results are provided in the Supplementary Dataset.

	Primary Visual Cortex	↑	16.9 [6.4,27.8]	0.999	↓	-4.0 [-6.6,-1.3]	0.998	↓	-5.7 [-10.2,-1.1]	0.990	↑	7.7 [4.4,11.0]	1.000
	MT+ Complex and Neighbouring Visual Areas	↑	19.6 [15.9,23.0]	1.000	↓	-3.8 [-4.5,-3.0]	1.000	↓	-2.3 [-3.7,-0.8]	0.999	↑	6.2 [5.1,7.2]	1.000
	Dorsal Stream Visual Cortex	↑	23.8 [18.9,28.6]	1.000	↓	-2.3 [-3.3,-1.4]	1.000	↓	-3.9 [-5.7,-2.0]	1.000	↑	6.1 [4.8,7.4]	1.000
	Early Visual Cortex	↑	9.4 [3.3,15.7]	0.999	↓	-3.2 [-4.5,-1.9]	1.000	↓	-4.2 [-6.7,-1.6]	1.000	↑	6.5 [4.9,8.2]	1.000
	Ventral Stream Visual Cortex		3.2 [-1.0,7.4]	0.928	↓	-1.1 [-2.0,-0.3]	0.993		-1.6 [-3.3,0.1]	0.962	↑	5.6 [4.4,6.7]	1.000
	Somatosensory and Motor Cortex	↑	6.2 [1.2,11.2]	0.994	↓	-2.2 [-3.2,-1.1]	1.000	↓	-4.4 [-6.5,-2.4]	1.000	↑	4.6 [3.3,6.0]	1.000
	Premotor Cortex	↑	19.0 [15.1,23.1]	1.000	↓	-2.1 [-3.0,-1.3]	1.000	↓	-5.4 [-7.1,-3.6]	1.000	↑	4.6 [3.4,5.7]	1.000
	Posterior Operculum		-1.0 [-5.6,3.3]	0.679		-0.5 [-1.4,0.4]	0.837	↓	-2.9 [-4.7,-1.2]	1.000	↑	3.4 [2.2,4.6]	1.000
	Paracentral Lobular and Mid Cingulate	↑	14.1 [10.1,18.1]	1.000	↓	-1.2 [-2.1,-0.4]	0.998	↓	-4.1 [-5.7,-2.5]	1.000	↑	3.8 [2.7,4.9]	1.000
	Early Auditory Cortex		1.9 [-3.1,6.9]	0.780		-0.1 [-1.1,0.9]	0.569	↓	-4.1 [-6.0,-2.1]	1.000	↑	2.4 [1.0,3.7]	1.000
	Auditory Association Cortex	↓	-5.3 [-9.4,-1.4]	0.997		-0.3 [-1.1,0.5]	0.784	↓	-2.5 [-4.0,-0.9]	0.998	↑	2.9 [1.8,3.9]	1.000
	Frontal Opercular and Insular Cortex	↑	6.5 [3.5,9.3]	1.000		-0.5 [-1.1,0.2]	0.920	↓	-3.6 [-4.8,-2.4]	1.000	↑	3.0 [2.2,3.9]	1.000
	Medial Temporal		-1.0 [-6.1,3.7]	0.669	↑	3.0 [1.8,4.0]	1.000		-1.0 [-2.9,1.0]	0.841	↑	1.4 [0.1,2.8]	0.983
	Lateral Temporal Cortex		-4.2 [-8.6,0.1]	0.972		-0.9 [-1.9,0.0]	0.972		-0.6 [-2.4,1.1]	0.739	↑	2.9 [1.7,4.2]	1.000
	Temporal-Parietal-Occipital Junction	↑	8.9 [4.4,14.0]	1.000		0.3 [-0.8,1.3]	0.698	↓	-3.0 [-5.0,-1.2]	0.998	↑	3.1 [1.8,4.5]	1.000
	Superior Parietal and IPS	↑	23.9 [20.4,27.4]	1.000	↓	-1.4 [-2.1,-0.6]	1.000	↓	-4.9 [-6.3,-3.4]	1.000	↑	3.7 [2.7,4.7]	1.000
	Inferior Parietal Cortex	↑	12.2 [8.5,15.6]	1.000	↓	-1.3 [-2.1,-0.5]	0.999	↓	-2.7 [-4.1,-1.3]	1.000	↑	3.5 [2.5,4.6]	1.000
	Posterior Cingulate		1.9 [-1.1,5.0]	0.890	↑	0.8 [0.2,1.4]	0.992		-1.1 [-2.3,0.1]	0.966	↑	3.0 [2.2,3.9]	1.000
	Anterior Cingulate		-0.1 [-3.1,2.8]	0.520		-0.4 [-1.1,0.3]	0.864	↓	-2.3 [-3.6,-1.1]	1.000	↑	3.5 [2.6,4.3]	1.000
	Orbital and Polar Frontal Cortex		-1.4 [-5.3,2.5]	0.760	↓	-1.5 [-2.4,-0.7]	0.999	↓	-2.3 [-4.0,-0.7]	0.998	↑	3.5 [2.4,4.6]	1.000
	Inferior Frontal Cortex	↑	5.4 [1.5,9.3]	0.999	↓	-0.9 [-1.8,-0.1]	0.989	↓	-2.2 [-3.8,-0.7]	0.997	↑	3.4 [2.4,4.4]	1.000
	Dorsolateral Prefrontal Cortex	↑	3.6 [0.6,6.8]	0.989		-0.6 [-1.3,0.0]	0.969	↓	-1.8 [-3.1,-0.7]	0.998	↑	2.9 [2.0,3.7]	1.000
	Thalamus	↑	11.0 [6.4,14.7]	1.000	↓	-1.1 [-2.0,-0.2]	0.989	↓	-3.6 [-5.3,-1.9]	1.000	↑	3.7 [2.6,4.8]	1.000
	Hypothalamus		7.5 [-0.5,15.2]	0.968		-0.3 [-1.9,1.3]	0.659	↓	-3.5 [-6.6,-0.4]	0.987	↑	2.3 [0.3,4.4]	0.990
	Striatum	↑	12.3 [8.2,16.4]	1.000	↓	-1.6 [-2.5,-0.8]	1.000	↓	-4.4 [-6.1,-2.8]	1.000	↑	4.3 [3.2,5.3]	1.000
	Pallidum	↑	11.4 [3.6,19.0]	0.997		-1.1 [-2.7,0.5]	0.919	↓	-4.0 [-6.9,-0.9]	0.993	↑	3.5 [1.5,5.6]	0.999
	Basal Ganglia-Associated Nuclei	↑	14.4 [6.3,21.7]	1.000		-0.8 [-2.5,0.9]	0.836	↓	-3.5 [-6.7,-0.5]	0.987		2.2 [0.0,4.5]	0.973
	Brainstem – Reticular and Sensorimotor Nuclei	↑	14.0 [6.9,21.1]	1.000		0.9 [-0.8,2.6]	0.850	↓	-5.2 [-8.1,-2.3]	1.000		1.3 [-0.7,3.3]	0.880
	Amygdala		-0.9 [-7.4,5.4]	0.608		0.4 [-1.1,1.9]	0.687	↓	-3.6 [-6.2,-0.9]	0.995	↑	2.4 [0.4,4.3]	0.990
	Hippocampus		-4.4 [-9.2,0.7]	0.952		-0.6 [-1.7,0.4]	0.890		0.9 [-1.0,2.9]	0.830	↑	1.9 [0.6,3.3]	0.997
	Cerebellum – Anterior Sensorimotor	↑	11.3 [3.4,19.4]	0.998	↓	-2.0 [-3.6,-0.4]	0.995		-2.7 [-5.7,0.4]	0.954	↑	3.1 [1.2,5.1]	0.999
	Cerebellum – VI (Transitional)	↑	19.2 [10.7,28.3]	1.000	↓	-2.5 [-4.7,-0.2]	0.983	↓	-4.8 [-9.0,-0.6]	0.989	↑	4.6 [2.0,7.4]	1.000
	Cerebellum – Executive/Associative	↑	11.5 [6.4,17.1]	1.000	↓	-3.6 [-4.7,-2.5]	1.000	↓	-2.2 [-4.4,-0.2]	0.983	↑	4.0 [2.6,5.5]	1.000
	Cerebellum – Sensorimotor VIII	↑	13.9 [7.6,20.4]	1.000	↓	-4.1 [-5.4,-2.7]	1.000		-1.6 [-4.2,1.0]	0.878	↑	5.3 [3.7,6.9]	1.000
	Cerebellum – Posterior (IX–X)	↑	10.9 [4.5,17.2]	1.000	↓	-2.3 [-3.6,-1.0]	1.000		-1.2 [-3.8,1.3]	0.827	↑	2.9 [1.2,4.6]	1.000
	Cerebellar Deep Nuclei		2.4 [-5.1,9.8]	0.746	↓	-2.0 [-3.6,-0.5]	0.994		-0.4 [-3.5,2.9]	0.600		1.8 [-0.3,3.7]	0.953

References

Aggarwal, Manisha, David W. Nauen, Juan C. Troncoso, and Susumu Mori. 2015. "Probing Region-Specific Microstructure of Human Cortical Areas Using High Angular and Spatial Resolution Diffusion MRI." *NeuroImage* 105 (January): 198–207. https://doi.org/10.1016/j.neuroimage.2014.10.053.

Andersson, Jesper L. R., Mark S. Graham, Ivana Drobnjak, Hui Zhang, and Jon Campbell. 2018. "Susceptibility-Induced Distortion That Varies Due to Motion: Correction in Diffusion MR without Acquiring Additional Data." *NeuroImage* 171 (May): 277–95. https://doi.org/10.1016/j.neuroimage.2017.12.040.

Andersson, Jesper L. R., Mark S. Graham, Ivana Drobnjak, Hui Zhang, Nicola Filippini, and Matteo Bastiani. 2017. "Towards a Comprehensive Framework for Movement and Distortion Correction of Diffusion MR Images: Within Volume Movement." *NeuroImage* 152: 450–66. https://doi.org/10.1016/j.neuroimage.2017.02.085.

Andersson, Jesper L. R., Mark S. Graham, Enikő Zsoldos, and Stamatios N. Sotiropoulos. 2016. "Incorporating Outlier Detection and Replacement into a Non-Parametric Framework for Movement and Distortion Correction of Diffusion MR Images." *NeuroImage* 141 (November): 556–72. https://doi.org/10.1016/j.neuroimage.2016.06.058.

Baladron, Javier, Julien Vitay, Torsten Fietzek, and Fred H. Hamker. 2023. "The Contribution of the Basal Ganglia and Cerebellum to Motor Learning: A Neuro-Computational Approach." *PLoS Computational Biology* 19 (4): e1011024. https://doi.org/10.1371/journal.pcbi.1011024.

Bar, Moshe. 2009. "Predictions: A Universal Principle in the Operation of the Human Brain. Introduction." *Philosophical Transactions of the Royal Society of London. Series B, Biological Sciences* 364 (1521): 1181–82. https://doi.org/10.1098/rstb.2008.0321.

Bareš, Martin, Richard Apps, Laura Avanzino, et al. 2019. "Consensus Paper: Decoding the Contributions of the Cerebellum as a Time Machine. From Neurons to Clinical Applications." *The Cerebellum* 18 (2): 266–86. https://doi.org/10.1007/s12311-018-0979-5.

Bares, Martin, Ovidiu V. Lungu, Tao Liu, Tobias Waechter, Christopher M. Gomez, and James Ashe. 2011. "The Neural Substrate of Predictive Motor Timing in Spinocerebellar Ataxia." *The Cerebellum* 10 (2): 233–44. 2011-12466-008. First Author & Affiliation: Bares, Martin, pp. 233–44. psyh. https://doi.org/10.1007/s12311-010-0237-y.

Barron, Helen C., Ryszard Auksztulewicz, and Karl Friston. 2020. "Prediction and Memory: A Predictive Coding Account." *Progress in Neurobiology* 192 (September): 101821. https://doi.org/10.1016/j.pneurobio.2020.101821.

Behrens, T. E. J., H. Johansen-Berg, M. W. Woolrich, et al. 2003. "Non-Invasive Mapping of Connections between Human Thalamus and Cortex Using Diffusion Imaging." *Nature Neuroscience* 6 (7): 750–57. https://doi.org/10.1038/nn1075.

Botvinick, Matthew M., Yael Niv, and Andew G. Barto. 2009. "Hierarchically Organized Behavior and Its Neural Foundations: A Reinforcement Learning Perspective." *Cognition* 113 (3): 262–80. https://doi.org/10.1016/j.cognition.2008.08.011.

Budde, Matthew D., and Jacopo Annese. 2013. "Quantification of Anisotropy and Fiber Orientation in Human Brain Histological Sections." *Frontiers in Integrative Neuroscience* 7 (February): 3. https://doi.org/10.3389/fnint.2013.00003.

Caligiore, Daniele, Michael A. Arbib, R. Chris Miall, and Gianluca Baldassarre. 2019a. "The Super-Learning Hypothesis: Integrating Learning Processes across Cortex, Cerebellum and Basal Ganglia." *Neuroscience & Biobehavioral Reviews* 100 (May): 19–34. https://doi.org/10.1016/j.neubiorev.2019.02.008.

Caligiore, Daniele, Michael A. Arbib, R. Chris Miall, and Gianluca Baldassarre. 2019b. "The Super-Learning Hypothesis: Integrating Learning Processes across Cortex, Cerebellum and Basal Ganglia." *Neuroscience and Biobehavioral Reviews* 100 (May): 19–34. https://doi.org/10.1016/j.neubiorev.2019.02.008.

Caligiore, Daniele, Giovanni Pezzulo, Gianluca Baldassarre, et al. 2017. "Consensus Paper: Towards a Systems-Level View of Cerebellar Function: The Interplay Between Cerebellum, Basal Ganglia, and Cortex." *Cerebellum (London, England)* 16 (1): 203–29. https://doi.org/10.1007/s12311-016-0763-3.

Clark, Andy. 2013. "Whatever next? Predictive Brains, Situated Agents, and the Future of Cognitive Science." *The Behavioral and Brain Sciences* 36 (3): 181–204. https://doi.org/10.1017/S0140525X12000477.

Conant, Roger C., and Ross W. Ashby. 1970. "Every Good Regulator of a System Must Be a Model of That System †." *International Journal of Systems Science* 1 (2): 89–97. https://doi.org/10.1080/00207727008920220.

Cordero-Grande, Lucilio, Daan Christiaens, Jana Hutter, Anthony N. Price, and Jo V. Hajnal. 2019. "Complex Diffusion-Weighted Image Estimation via Matrix Recovery under General Noise Models." *NeuroImage* 200 (October): 391–404. https://doi.org/10.1016/j.neuroimage.2019.06.039.

Davis, D. G., M. E. Perlman, and R. E. London. 1994. "Direct Measurements of the Dissociation-Rate Constant for Inhibitor-Enzyme Complexes via the T1 Rho and T2 (CPMG) Methods." *Journal of Magnetic Resonance. Series B* 104 (3): 266–75. https://doi.org/10.1006/jmrb.1994.1084.

Davison, M., and J. Nevin. 1999. "Stimuli, Reinforcers, and Behavior: An Integration." *Journal of the Experimental Analysis of Behavior* 71 (3): 439–82. https://doi.org/10.1901/jeab.1999.71-439.

Den Ouden, Hanneke EM, Peter Kok, and Floris P. De Lange. 2012. "How Prediction Errors Shape Perception, Attention, and Motivation." *Frontiers in Psychology* 3 (December). https://doi.org/10.3389/fpsyg.2012.00548.

Dercksen, Tjerk T., Andreas Widmann, Tömme Noesselt, and Nicole Wetzel. 2024. "Somatosensory Omissions Reveal Action-Related Predictive Processing." *Human Brain Mapping* 45 (4): e26550. https://doi.org/10.1002/hbm.26550.

Diedrichsen, J., J. H. Balsters, J. Flavell, E. Cussans, and N. Ramnani. 2009. "A Probabilistic MR Atlas of the Human Cerebellum." *NeuroImage* 46 (1): 39–46. https://doi.org/10.1016/j.neuroimage.2009.01.045.

Doya, K. 2000. "Complementary Roles of Basal Ganglia and Cerebellum in Learning and Motor Control." *Current Opinion in Neurobiology* 10 (6): 732–39. https://doi.org/10.1016/s0959-4388(00)00153-7.

Edlow, Brian L., Emi Takahashi, Ona Wu, et al. 2012. "Neuroanatomic Connectivity of the Human Ascending Arousal System Critical to Consciousness and Its Disorders." *Journal of Neuropathology and Experimental Neurology* 71 (6): 531–46. https://doi.org/10.1097/NEN.0b013e3182588293.

Filip, Pavel, Cécile Gallea, Stéphane Lehéricy, et al. 2017. "Disruption in Cerebellar and Basal Ganglia Networks during a Visuospatial Task in Cervical Dystonia." *Movement Disorders: Official Journal of the Movement Disorder Society* 32 (5): 757–68. https://doi.org/10.1002/mds.26930.

Filip, Pavel, Cécile Gallea, Stéphane Lehéricy, Ovidiu Lungu, and Martin Bareš. 2019. "Neural Scaffolding as the Foundation for Stable Performance of Aging Cerebellum." *The Cerebellum*, ahead of print, March 2. https://doi.org/10.1007/s12311-019-01015-7.

Filip, Pavel, Jan Lošák, Tomáš Kašpárek, Jiří Vaníček, and Martin Bareš. 2016. "Neural Network of Predictive Motor Timing in the Context of Gender Differences." *Neural Plasticity* 2016.

Fischer, M. W., L. Zeng, A. Majumdar, and E. R. Zuiderweg. 1998. "Characterizing Semilocal Motions in Proteins by NMR Relaxation Studies." *Proceedings of the National Academy of Sciences of the United States of America* 95 (14): 8016–19. https://doi.org/10.1073/pnas.95.14.8016.

Friston, K. J., A. P. Holmes, K. J. Worsley, J.-P. Poline, C. D. Frith, and R. S. J. Frackowiak. 1994. "Statistical Parametric Maps in Functional Imaging: A General Linear Approach." *Human Brain Mapping* 2 (4): 189–210. https://doi.org/10.1002/hbm.460020402.

Friston, Karl. 2010. "The Free-Energy Principle: A Unified Brain Theory?" *Nature Reviews. Neuroscience* 11 (2): 127–38. https://doi.org/10.1038/nrn2787.

Fu, Min, and Yi Zuo. 2011. "Experience-Dependent Structural Plasticity in the Cortex." *Trends in Neurosciences* 34 (4): 177–87. https://doi.org/10.1016/j.tins.2011.02.001.

Garwood, Michael, and Lance DelaBarre. 2001. "The Return of the Frequency Sweep: Designing Adiabatic Pulses for Contemporary NMR." *Journal of Magnetic Resonance* 153 (2): 155–77.

Gelman, Andrew, John B. Carlin, Hal S. Stern, David B. Dunson, Akti Vehtari, and Donald B. Rubin. 2013. *Bayesian Data Analysis*. Third. Chapman & Hall/CRC Texts in Statistical Science Series. CRC. https://stat.columbia.edu/~gelman/book/.

Gelman, Andrew, Jennifer Hill, and Masanao Yajima. 2012. "Why We (Usually) Don't Have to Worry About Multiple Comparisons." *Journal of Research on Educational Effectiveness* 5 (2): 189–211. https://doi.org/10.1080/19345747.2011.618213.

Glasser, Matthew F., Timothy S. Coalson, Emma C. Robinson, et al. 2016. "A Multi-Modal Parcellation of Human Cerebral Cortex." *Nature* 536 (7615): 171–78.

Glasser, Matthew F., Stamatios N. Sotiropoulos, J. Anthony Wilson, et al. 2013. "The Minimal Preprocessing Pipelines for the Human Connectome Project." *Neuroimage* 80: 105–24. https://doi.org/10.1016/j.neuroimage.2013.04.127.

Harms, Michael P., Leah H. Somerville, Beau M. Ances, et al. 2018. "Extending the Human Connectome Project across Ages: Imaging Protocols for the Lifespan Development and Aging Projects." *NeuroImage* 183 (December): 972–84. https://doi.org/10.1016/j.neuroimage.2018.09.060.

Hull, Court. 2020. "Prediction Signals in the Cerebellum: Beyond Supervised Motor Learning." *eLife* 9 (March): e54073. https://doi.org/10.7554/eLife.54073.

Hund-Georgiadis, M., and D. Y. von Cramon. 1999. "Motor-Learning-Related Changes in Piano Players and Non-Musicians Revealed by Functional Magnetic-Resonance Signals." *Experimental Brain Research* 125 (4): 417–25. https://doi.org/10.1007/s002210050698.

Jäncke, L., N. J. Shah, and M. Peters. 2000. "Cortical Activations in Primary and Secondary Motor Areas for Complex Bimanual Movements in Professional Pianists." *Brain Research. Cognitive Brain Research* 10 (1–2): 177–83. https://doi.org/10.1016/s0926-6410(00)00028-8.

Jeurissen, Ben, Jacques-Donald Tournier, Thijs Dhollander, Alan Connelly, and Jan Sijbers. 2014. "Multi-Tissue Constrained Spherical Deconvolution for Improved Analysis of Multi-Shell Diffusion MRI Data." *NeuroImage* 103: 411–26.

Kamiya, Kouhei, Masaaki Hori, and Shigeki Aoki. 2020. "NODDI in Clinical Research." *Journal of Neuroscience Methods* 346: 108908.

Kellner, Elias, Bibek Dhital, Valerij G. Kiselev, and Marco Reisert. 2016. "Gibbs-Ringing Artifact Removal Based on Local Subvoxel-Shifts." *Magnetic Resonance in Medicine* 76 (5): 1574–81.

Keuken, M. C., P.-L. Bazin, K. Backhouse, et al. 2017. "Effects of Aging on T_1, T_2*, and QSM MRI Values in the Subcortex." *Brain Structure & Function* 222 (6): 2487–505. https://doi.org/10.1007/s00429-016-1352-4.

Korka, Betina, Andreas Widmann, Florian Waszak, Álvaro Darriba, and Erich Schröger. 2022. "The Auditory Brain in Action: Intention Determines Predictive Processing in the Auditory System—A Review of Current Paradigms and Findings." *Psychonomic Bulletin & Review* 29 (2): 321–42. https://doi.org/10.3758/s13423-021-01992-z.

Lehmann, Nico, Norman Aye, Jörn Kaufmann, et al. 2023. "Changes in Cortical Microstructure of the Human Brain Resulting from Long-Term Motor Learning." *The Journal of Neuroscience: The Official Journal of the Society for Neuroscience* 43 (50): 8637–48. https://doi.org/10.1523/JNEUROSCI.0537-23.2023.

Levitt, Malcolm H., Ray Freeman, and Thomas Frenkiel. 1982. "Broadband Heteronuclear Decoupling." *Journal of Magnetic Resonance (1969)* 47 (2): 328–30.

Lindgren, Finn, and Håvard Rue. 2015. "Bayesian Spatial Modelling with R-INLA." Articles. *Journal of Statistical Software* 63 (19): 1–25. https://doi.org/10.18637/jss.v063.i19.

Marková, Lenka, Martin Bareš, Ovidiu V. Lungu, and Pavel Filip. 2020. "Quantitative but Not Qualitative Performance Changes in Predictive Motor Timing as a Result of Overtraining." *Cerebellum (London, England)* 19 (2): 201–7. https://doi.org/10.1007/s12311-019-01100-x.

Matteucci, Giulio, Eugenio Piasini, and Davide Zoccolan. 2024. "Unsupervised Learning of Mid-Level Visual Representations." *Current Opinion in Neurobiology* 84 (February): 102834. https://doi.org/10.1016/j.conb.2023.102834.

Meister, Ingo, Timo Krings, Henrik Foltys, et al. 2005. "Effects of Long-Term Practice and Task Complexity in Musicians and Nonmusicians Performing Simple and Complex Motor Tasks: Implications for Cortical Motor Organization." *Human Brain Mapping* 25 (3): 345–52. https://doi.org/10.1002/hbm.20112.

Mejia, Amanda F., Yu Ryan Yue, David Bolin, Finn Lindgren, and Martin A. Lindquist. 2020. "A Bayesian General Linear Modeling Approach to Cortical Surface fMRI Data Analysis." *Journal of the American Statistical Association* 115 (530): 501–20. https://doi.org/10.1080/01621459.2019.1611582.

Michaeli, Shalom, Terry C. Burns, Elina Kudishevich, et al. 2009. "Detection of Neuronal Loss Using T1ρ MRI Assessment of 1H2O Spin Dynamics in the Aphakia Mouse." *Journal of Neuroscience Methods* 177 (1): 160–67.

Michaeli, Shalom, Dennis J. Sorce, Charles S. Springer Jr, Kamil Ugurbil, and Michael Garwood. 2006. "T1ρ MRI Contrast in the Human Brain: Modulation of the Longitudinal Rotating Frame Relaxation Shutter-Speed during an Adiabatic RF Pulse." *Journal of Magnetic Resonance* 181 (1): 135–47.

Młynarski, Wiktor, and Gašper Tkačik. 2022. "Efficient Coding Theory of Dynamic Attentional Modulation." *PLoS Biology* 20 (12): e3001889. https://doi.org/10.1371/journal.pbio.3001889.

Pezzulo, Giovanni, Thomas Parr, and Karl Friston. 2022. "The Evolution of Brain Architectures for Predictive Coding and Active Inference." *Philosophical Transactions of the Royal Society of London. Series B, Biological Sciences* 377 (1844): 20200531. https://doi.org/10.1098/rstb.2020.0531.

Pezzulo, Giovanni, Francesco Rigoli, and Karl Friston. 2015. "Active Inference, Homeostatic Regulation and Adaptive Behavioural Control." *Progress in Neurobiology* 134 (November): 17–35. https://doi.org/10.1016/j.pneurobio.2015.09.001.

Picard, Nathalie, Yoshiya Matsuzka, and Peter L. Strick. 2013. "Extended Practice of a Motor Skill Is Associated with Reduced Metabolic Activity in M1." *Nature Neuroscience* 16 (9): 1340–47. https://doi.org/10.1038/nn.3477.

Powers, William T. 1973. "Behavior, the Control of Perception." https://api.semanticscholar.org/CorpusID:145556271.

Raymond, Jennifer L., Stephen G. Lisberger, and Michael D. Mauk. 1996. "The Cerebellum: A Neuronal Learning Machine?" *Science* 272 (5265): 1126–31.

Roo, Mathias De, Paul Klauser, and Dominique Muller. 2008. "LTP Promotes a Selective Long-Term Stabilization and Clustering of Dendritic Spines." *PLOS Biology* 6 (9): e219. https://doi.org/10.1371/journal.pbio.0060219.

Schifani, Christin, Colin Hawco, Arash Nazeri, and Aristotle N. Voineskos. 2022. "Relationship of Neurite Architecture to Brain Activity during Task-Based fMRI." *NeuroImage* 262 (November): 119575. https://doi.org/10.1016/j.neuroimage.2022.119575.

Smith, Robert E., Jacques-Donald Tournier, Fernando Calamante, and Alan Connelly. 2012. "Anatomically-Constrained Tractography: Improved Diffusion MRI Streamlines Tractography through Effective Use of Anatomical Information." *Neuroimage* 62 (3): 1924–38.

Smith, Robert E., Jacques-Donald Tournier, Fernando Calamante, and Alan Connelly. 2015. "SIFT2: Enabling Dense Quantitative Assessment of Brain White Matter Connectivity Using Streamlines Tractography." *Neuroimage* 119: 338–51.

Smith, Stephen M., Christian F. Beckmann, Jesper Andersson, et al. 2013. "Resting-State fMRI in the Human Connectome Project." *Neuroimage* 80: 144–68. https://doi.org/10.1016/j.neuroimage.2013.05.039.

Spindler, Melanie, Jale Özyurt, and Christiane M. Thiel. 2020. "Automated Diffusion-Based Parcellation of the Hypothalamus Reveals Subunit-Specific Associations with Obesity." *Scientific Reports* 10 (1): 22238. https://doi.org/10.1038/s41598-020-79289-9.

Tanaka, Hirokazu, Takahiro Ishikawa, Jongho Lee, and Shinji Kakei. 2020. "The Cerebro-Cerebellum as a Locus of Forward Model: A Review." *Frontiers in Systems Neuroscience* 14 (April). https://doi.org/10.3389/fnsys.2020.00019.

Tariq, Maira, Torben Schneider, Daniel C. Alexander, Claudia A. Gandini Wheeler-Kingshott, and Hui Zhang. 2016. "Bingham–NODDI: Mapping Anisotropic Orientation Dispersion of Neurites Using Diffusion MRI." *NeuroImage* 133 (June): 207–23. https://doi.org/10.1016/j.neuroimage.2016.01.046.

Tavor, Ido, Shir Hofstetter, and Yaniv Assaf. 2013. "Micro-Structural Assessment of Short Term Plasticity Dynamics." *NeuroImage* 81 (November): 1–7. https://doi.org/10.1016/j.neuroimage.2013.05.050.

Tsay, Jonathan S., Adrian M. Haith, Richard B. Ivry, and Hyosub E. Kim. 2022. "Interactions between Sensory Prediction Error and Task Error during Implicit Motor Learning." *PLoS Computational Biology* 18 (3): e1010005. https://doi.org/10.1371/journal.pcbi.1010005.

Tziortzi, Andri C., Suzanne N. Haber, Graham E. Searle, et al. 2014. "Connectivity-Based Functional Analysis of Dopamine Release in the Striatum Using Diffusion-Weighted MRI and Positron Emission Tomography." *Cerebral Cortex* 24 (5): 1165–77. https://doi.org/10.1093/cercor/bhs397.

Veraart, Jelle, Els Fieremans, and Dmitry S. Novikov. 2016. "Diffusion MRI Noise Mapping Using Random Matrix Theory." *Magnetic Resonance in Medicine* 76 (5): 1582–93.

Winkler, Anderson M., Gerard R. Ridgway, Matthew A. Webster, Stephen M. Smith, and Thomas E. Nichols. 2014. "Permutation Inference for the General Linear Model." *NeuroImage* 92 (May): 381–97. https://doi.org/10.1016/j.neuroimage.2014.01.060.

Winterburn, Julie L., Jens C. Pruessner, Sofia Chavez, et al. 2013. "A Novel in Vivo Atlas of Human Hippocampal Subfields Using High-Resolution 3 T Magnetic Resonance Imaging." *NeuroImage* 74 (July): 254–65. https://doi.org/10.1016/j.neuroimage.2013.02.003.

Supplementary Methods

Second-level hierarchical model (full formula)

Indices and data

Let

- $m = 1, \ldots, M$ index participants (M = 87),
- $s = 1, \ldots, S$ index sessions (S = 3),
- $p = 1, \ldots, P$ index parcels (P = 432),
- $k = 1, \ldots, K$ index planned contrasts (K = 4)
    - shooting–cross difference across all speed levels,
    - linear speed scaling of the shooting–cross difference,
    - shooting–cross difference in timing-error modulation,
    - linear speed scaling of shooting–cross difference in timing-error modulation
- $c(p) \in \{1, \ldots, C\}$ anatomical clique of parcel p (C = 37, see Supplementary Table 1).

INLA inputs to the second level group model are the session- and parcel-wise contrast estimates and their propagated uncertainties:

- $\hat{\beta}_{mspk}$ = first-level (INLA) posterior mean of contrast k for participant m, session s, parcel p.
- SE_{mspk}= propagated posterior standard deviation for that contrast based on the full posterior covariance tensor of first-level coefficients.

Participant/session predictors:

- $G_m \in \{expert, control\}$: group indicator
- A_m: age (centred and scaled)
- $X_m \in \{male, female\}$: sex indicator
- $t_s \in \{-1, 0, 1\}$: centred session code (linear practice trend)

The second level was a multivariate model over all contrasts: k = 1, …, K were estimated jointly in one model with contrast-specific parameters $(\cdot)_k$ and shared hierarchical structure across parcels/cliques, but with contrast-specific parameters and conditionally independent likelihood across contrasts.

Observation model (measurement-error likelihood)

For every m, s, p, k:

$$\hat{\beta}_{mspk} \sim \mathcal{N}\left(\mu_{mspk}, \mathrm{SE}^2_{mspk} + \sigma^2_{\mathrm{add},k}\right),$$

where $\sigma_{\mathrm{add},k} \geq 0$ reflects extra second-level variability over the propagated first-level uncertainty.

Linear predictor with clique pooling

Clique-level coefficient matrices were defined for each contrast k as follows:

- control-group mean effect at t = 0: $\alpha_{0,ck}$ (parameterised at the exposure level centred to the middle session (t = 0) to improve interpretability; all parameters were estimated jointly using data from all three sessions).
- expert–control difference at t = 0: $\alpha_{G,ck}$
- linear session trend in controls: $\alpha_{S,ck}$

- group-by-session interaction: $\alpha_{GS,ck}$
- age effect (clique-only): $\alpha_{A,ck}$
- sex effect (clique-only): $\alpha_{X,ck}$

Furthermore, parcel-level deviation was added for the following terms:

- unstructured deviations for control-group mean effect and expert-control difference: $\varepsilon_{pk}^{(0)}$, $\varepsilon_{pk}^{(G)}$
- deviations for session terms: $\delta_{pk}^{(S)}$, $\delta_{pk}^{(GS)}$

with hierarchical scales controlling the extent of parcel-level deviations around clique-level pooled effects (contrast-specific, non-negative; smaller values imply stronger pooling): $\sigma_{\varepsilon 0,k}$, $\sigma_{\varepsilon G,k}$, $\sigma_{\delta S,k}$, $\sigma_{\delta GS,k}$.

Then the mean for each observation, estimating all planned contrasts $k = 1, \ldots, K$ under the same hierarchical structure, was:

$$\mu_{mspk} = \underbrace{\left(\alpha_{0,ck}+\sigma_{\varepsilon 0,k}\,\varepsilon_{pk}^{(0)}\right)}_{\text{control-group mean effect}} + \underbrace{\left(\alpha_{G,ck}+\sigma_{\varepsilon G,k}\,\varepsilon_{pk}^{(G)}\right)G_m}_{\text{expert-control difference}} + \underbrace{\left(\alpha_{S,ck}+\sigma_{S,k}\,z_{pk}^{(S)}\right)t_s}_{\text{linear session trend}} + \underbrace{\left(\alpha_{GS,ck}+\sigma_{GS,k}\,z_{pk}^{(GS)}\right)(G_m\,t_s)}_{\text{group-by-session interaction}} + \underbrace{\alpha_{A,c(p)k}A_m + \alpha_{X,c(p)k}X_m}_{\text{age/sex adjustment}}$$

Priors

Weakly informative priors were utilised, independently across contrasts *k:*

- For all cliques *c* and contrasts *k*: $\alpha_{\cdot,ck} \sim \mathcal{N}(0,1)$ for $\cdot \in \{0, G, S, GS, A, X\}$.
- Parcel-level latent deviations: $\varepsilon_{pk}^{(0)}$, $\varepsilon_{pk}^{(G)}$, $\delta_{pk}^{(S)}$, $\delta_{pk}^{(GS)} \sim \mathcal{N}(0,1)$.
- Hierarchical scales and the additional residual (weakly informative scale considering the structural connectome-based spatial regularisation on parcel-wise effects in the first-level INLA model): $\sigma_{\varepsilon 0,k}$, $\sigma_{\varepsilon G,k}$, $\sigma_{\delta S,k}$, $\sigma_{\delta GS,k}$, $\sigma_{\text{add},k} \sim \mathcal{N}^{+}(0,0.2)$

Robustness analysis of clique-pooling

To address potential concern of the hierarchical models overly favouring clique-level structure, an alternative model was fitted with explicitly prioritised parcel-level effects via an estimated clique-weight controlling the extent of clique-level pooling. Specifically, the parcel-level parameter was modelled as a convex combination of the clique component and an independent parcel component:

$$\mu_{\cdot p,k} = \kappa_{\cdot}\, a_{c(p),k} + (1 - \kappa_{\cdot})\, b_{\cdot p,k}$$

where $a_{c(p),k}$ stands for clique-level effects, $b_{p,k}$ parcel-level effects, and $\kappa \in [0,1]$ is an estimated weighting factor of clique influence. Furthermore, priors on $\kappa \sim \beta(1,9)$ strongly favoured weak clique contributions by default (mean 0.10), so that parcel-level resolution would collapse to clique-dominant outcome only if strongly supported by the data. The other parameters were retained from the primary model.

This robustness model produced spatial patterns and outcomes virtually identical to the primary hierarchical model, with very low posterior estimates of clique weights in the expert–control effect (κ_G posterior mean ≈ 0.0026, 5th–95th percentile ≈ 0.0023–0.0029; $\hat{R} \approx 1.01$). Ergo, the model did not primarily rely on explicit clique pooling. However, parcel-specific deviations were still strongly shrunk towards zero and clique component explained the majority of the group-effect posterior mass (mean share of clique contribution ≈ 0.95; 5th – 95th percentile ≈ 0.884–0.996). While this apparent dominance of lower granularity of anatomical resolution may genuinely reflect a smooth biological effect, another explanation may lie in the insufficient sensitivity at parcel resolution (effective sample size, temporal signal-to-noise ratio) where available dataset cannot support inferences at higher resolution.

Comparison against Legacy Pipelines

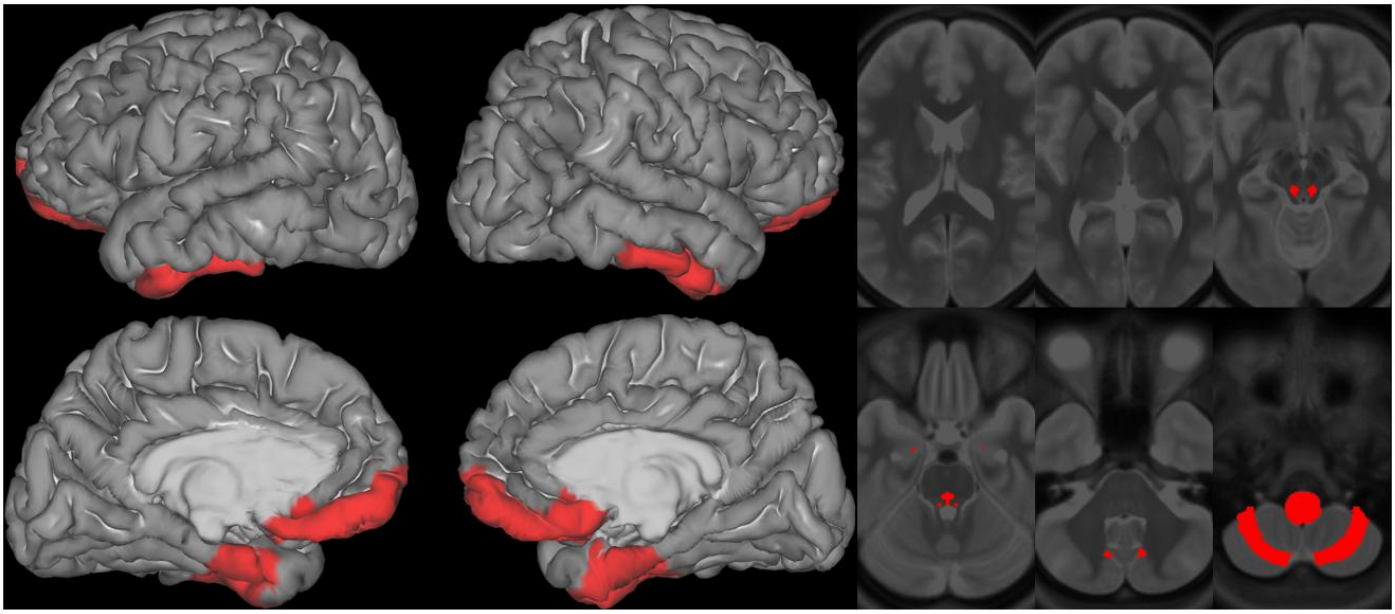
To validate activation patterns detectable using the proposed Bayesian pipeline, a legacy-style analysis was performed restricted to the cohort-level task effect (shooting–cross averaged across speed levels and across all three task fMRI sessions) corresponding to the previously published "Positive Effect of Task" (Filip et al. 2017). Three complementary analyses were performed:

- SPM-style mass univariate voxel-wise analysis in MNI space using HCP-pipeline volumetric output and common spatial smoothing approach (8mm isotropic Gaussian kernel), with first and second-level models estimated in SPM12 (Friston et al. 1994) using default settings as in our previous publication (Filip et al. 2017)
- Parcellated analysis, mass univariate analysis over 432 parcels passing QC described in the main text, first-level model in SPM12 (no global normalisation, AR(1), masking threshold 0.8, no interactions terms, canonical HRF convolution), second-level inference via PALM (10,000 permutations) (Winkler et al. 2014).
- simplified Bayesian model retaining structural connectome regularised first-level INLA estimation, uncertainty propagation and clique pooling, but limited at the second level to single legacy task-effect contrast.

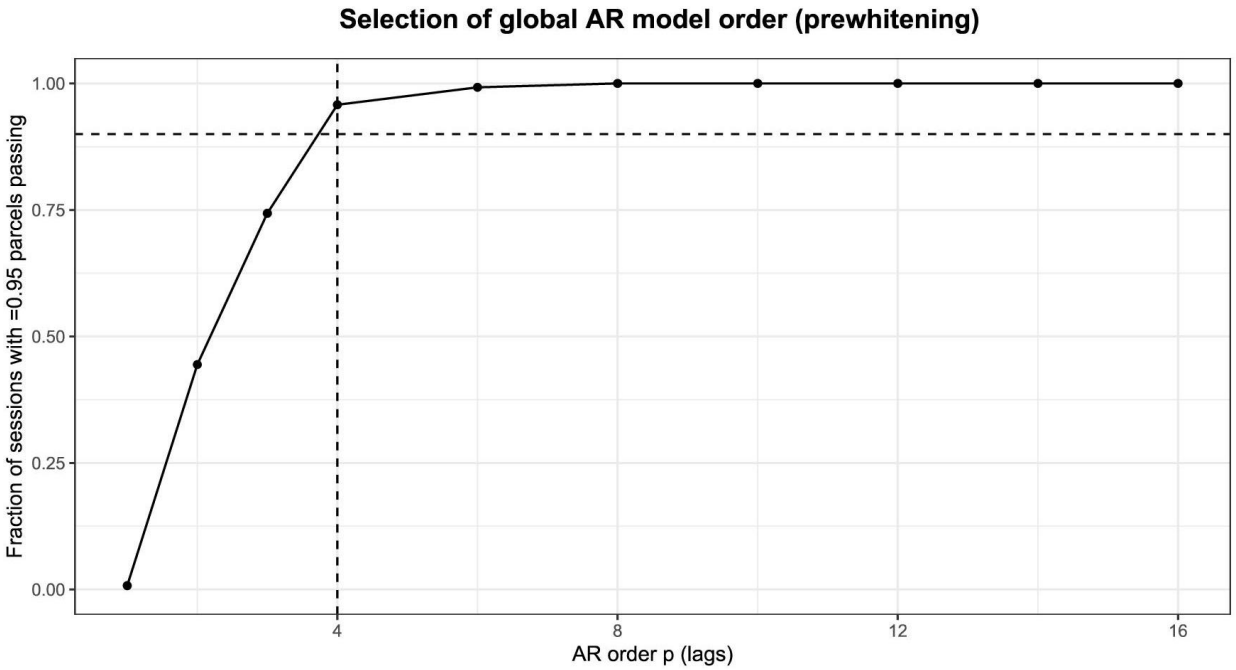
The frequentist models implemented standard significance threshold of $\alpha=0.05$ with family-wise error correction (voxel/parcel-level) for multiple comparisons due to the large number of independent tests ($>1.5\times10^5$ non-zero voxels within SPM-derived study-specific brain mask; 432 parcels). In contrast, joint estimation with partial pooling in Bayesian hierarchical models inherently shrinks extreme estimates towards group-level distribution, thereby mitigating multiplicity concerns (Gelman et al. 2012). Descriptive localisation for the Bayesian model was thresholded at 95% central credible interval – i.e. posterior sign probability of 97.5% ($\max [P(\theta > 0), P(\theta < 0)] \geq 0.975$), corresponding to the frequentist two-sided 5% convention (Gelman et al. 2013).

Supplementary Figures

Supplementary Figure 1: Parcels excluded based on multivariate parcel-level quality control procedure. Excluded regions were located primarily in the orbitofrontal and polar frontal cortex, anterior cingulate cortex, lateral and medial temporal cortex (including entorhinal and perirhinal areas), brainstem, cerebellar lobule VIIIa, and the basolateral ventral amygdala. Subcortical structures presented in 6 slices z = 16, 2, -12, -26, -40, -54 (Montreal Neurological Institute space), consistent with subsequent figures. Laterality convention follows radiological standards (the right side of the image corresponds to the right side of the brain).

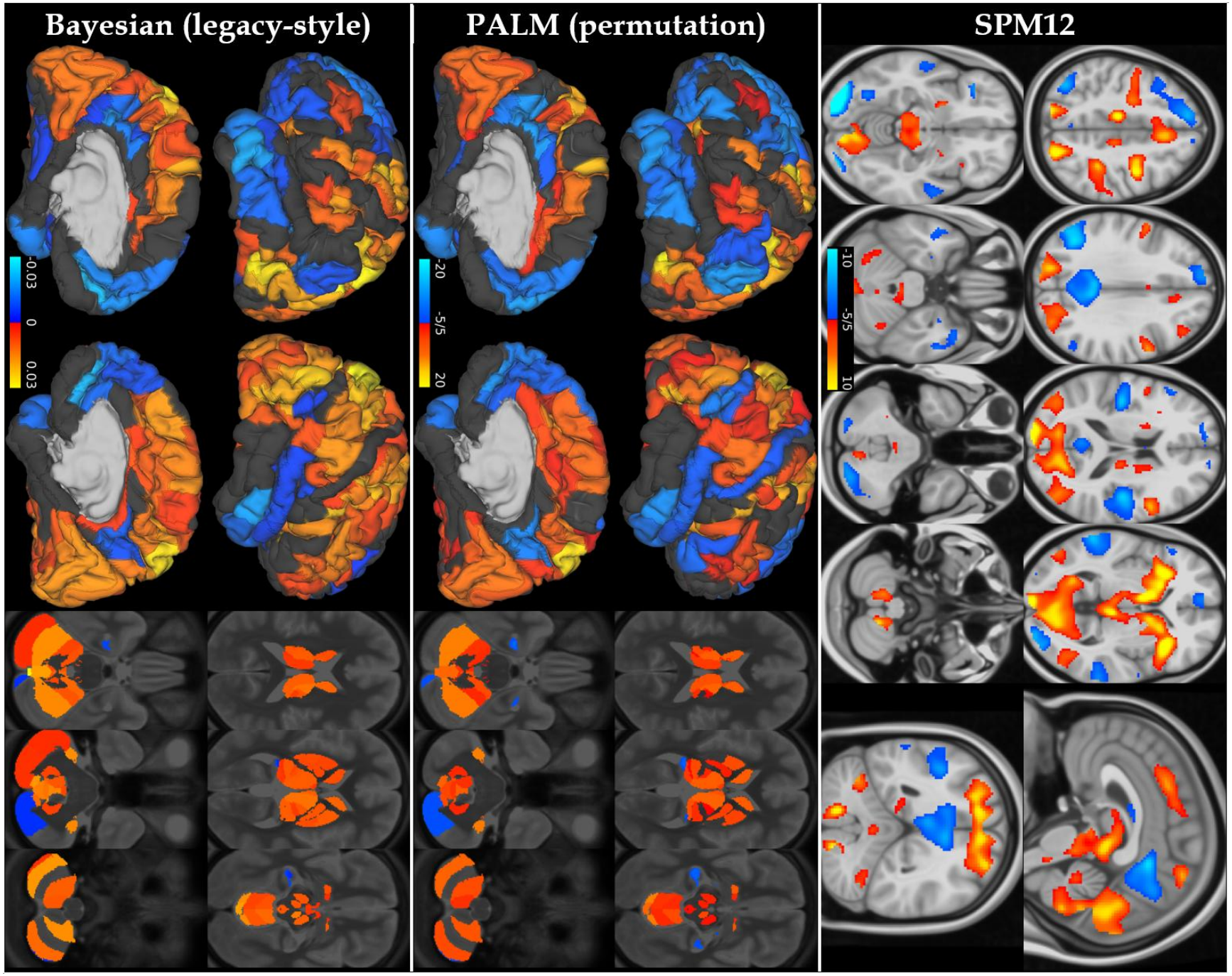


Supplementary Figure 2: Selection of the global autoregression (AR) order for temporal prewhitening, based on session-wise assessment of candidate AR orders (p) using Ljung–Box tests (lag 24), with Benjamini–Hochberg correction across parcels within each session (FDR-adjusted α = 0.05). The curve corresponds to the fraction of sessions with at least 95% of parcels meeting the whiteness criterion. The dashed horizontal line marks the prespecified target (≥0.90 of sessions); the dashed vertical line indicates the selected order (AR(4), i.e. the smallest p meeting the criterion).



Supplementary Figure 3: Comparison against legacy pipelines (voxel/parcel-wise frequentist approach). Whole-cohort task-related contrast (shooting–cross averaged over speeds and sessions at each subject's first-level model). SPM12 (mass-univariate voxel-wise analysis in standard space) and mainly PALM (mass-univariate parcel-level analysis) provided highly consistent cortical and subcortical activation patterns as the Bayesian pipeline. Subcortical effects included increase in striatal, thalamic and cerebellar activity, including the replication of right crus II decrease in otherwise relatively symmetric settings. Cortical effects showed increased activity in premotor, superior temporal, visual and dorsolateral prefrontal cortex and decreases in cingulate, frontal polar and lateral temporal cortex. The close correspondence between PALM and Bayesian activation patterns reflects high robustness of the task-related contrast at the level of the whole cohort, driving mass-univariate inference towards near-ceiling significance. Simple thresholding then collapses calibrated effect estimates and uncertainty quantification provided by the Bayesian pipeline, which are shown to be essential in the primary analyses in the main text.

SPM12 and PALM maps displayed using the common convention overlaying two separate positive and negative directional contrasts thresholded at $p<0.05$ (one-sided; union of tails) for pattern comparison. Bayesian results thresholded using posterior sign probability ≥0.95 (sign-symmetric by construction; roughly analogous to two-sided $p\approx0.05$ threshold; though not mathematically equivalent to frequentist tail probability). SPM12 results presented in 8 axial slices (z = 44, 30, 16, 2, -12, -26, -40, -54), a midline sagittal (x = 0) and coronal slice at the level of the cerebellum (y =-52) (Montreal Neurological Institute space). Parcellated results shown in combined cerebral surface reconstructions with subcortical standard space in 6 slices (z = 16, 2, -12, -26, -40, -54), consistent with main figures. Laterality follows radiological convention (the right side of the image corresponds to the right side of the brain). Full numerical results underlying the figures are provided in the Supplementary Dataset.


Bayesian (legacy-style)
PALM (permutation)
SPM12
-0.03
0
0.03
-20
-5/5
20
-10
-5/5
10

Supplementary Tables

Supplementary Table 1: Overarching anatomical segments used to define parcel groupings for clique-based hierarchies in the second-level Bayesian models. All parcels within each segment were partially pooled via clique-level effects with separately modelled parcel-level deviations.

1	Primary Visual Cortex	2	**Visual/ Occipital Cortex**	Human Connectome Project Multimodal Parcellation Atlas *(Glasser et al. 2016)*
2	MT+ Complex and Neighbouring Visual Areas	18		
3	Dorsal Stream Visual Cortex	12		
4	Early Visual Cortex	6		
5	Ventral Stream Visual Cortex	14		
6	Somatosensory and Motor Cortex	10	**Sensori-motor Cortex**	
7	Premotor Cortex	14		
8	Posterior Opercular Cortex	12		
9	Paracentral Lobular and Mid Cingulate Cortex	16		
10	Early Auditory Cortex	10	**Auditory Cortex**	
11	Auditory Association Cortex	16		
12	Frontal Opercular and Insular Cortex	26		
13	Medial Temporal	14	**Temporal Cortex**	
14	Lateral Temporal Cortex	18		
15	Temporal-Parietal-Occipital Junction	10	**Parietal Cortex**	
16	Superior Parietal and IPS	20		
17	Inferior Parietal Cortex	20		
18	Posterior Cingulate Cortex	28		
19	Anterior Cingulate and Medial Prefrontal Cortex	30	**Frontal Cortex**	
20	Orbital and Polar Frontal Cortex	22		
21	Inferior Frontal Cortex	16		
22	Dorsolateral Prefrontal Cortex	26		
23	Thalamus	14	**Dience-phalon**	Oxford Thalamic Connectivity Probability Atlas *(Behrens et al. 2003)*
24	Hypothalamus	4		Hypothalamic atlas *(Spindler et al. 2020)*
25	Striatum	14	**Basal Ganglia**	Oxford-Imanova Striatal Atlas *(Tziortzi et al. 2014)*
26	Pallidum	4		ATAG for middle aged, elderly *(Keuken et al. 2017)*
27	Basal Ganglia-Associated Nuclei	4		
28	Brainstem – Monoaminergic and Arousal Nuclei	3	**Brainstem**	Harvard Ascending Arousal Network Atlas *(Edlow et al. 2012)*
29	Brainstem – Reticular and Sensorimotor Integration Nuclei	7		
30	Amygdala	10	**Limbic System**	High-resolution atlas of amygdala *(Saygin et al. 2017)*
31	Hippocampus	10		In Vivo High-Resolution Atlas of the Hippocampus and Subfields *(Winterburn et al. 2013)*
32	Cerebellar Cortex – Anterior Sensorimotor	4	**Cerebellum**	Probabilistic structural cerebellar atlas *(Dietrichsen et al. 2009)*
33	Cerebellar Cortex – VI (Transitional)	3		
34	Cerebellar Cortex – Executive/Associative	8		
35	Cerebellar Cortex – Sensorimotor VIII	6		
36	Cerebellar Cortex – Posterior (IX–X)	6		
37	Cerebellar Deep Nuclei	4		

Supplementary Table 2: Convergence diagnostics and sampler behaviour of second-level Bayesian models for the main effects of interest. $\hat{R}$ denotes the Gelman–Rubin convergence diagnostic; ESS effective sample size. Bulk ESS and tail ESS provide summaries of sampling efficiency for the bulk of the posterior distribution and for tail quantities (e.g. credible interval endpoints), respectively. Worst-case values across the main effects of interest are reported (minimum ESS; maximum $\hat{R}$).

Main task-fMRI model	1.009	2,261	1,328	0	0
Microstructural group-level comparison	1.005	2,119	1,711	0	0

Supplementary Table 3: Results of second level task-related activation effects for motor prediction (shooting–cross) **and error modulation (**within the same contrast). Corresponding spatial maps provided in the Figure 3. Reported over larger anatomical partitions (cliques, see also Supplementary Table 1) separately for control-group mean effect and expert–control difference. Values provided as posterior medians with 95% credible intervals (CrI) (multiplied by 10^3 for numerical clarity) and posterior probability that the effect has the reported sign (P(sign)). Arrows indicate effects whose 95% CrI excludes zero (↑ positive, ↓ negative); effects with CrI spanning zero shown in grey. The ordering of cliques follows anatomical hierarchies across cortical, subcortical and cerebellar systems. Full numerical parcellated results are provided in the Supplementary Dataset.

	Primary Visual Cortex	↑	5.6 [1.6,9.5]	0.998	↓	-8.8 [-12.2,-5.2]	1.000	↓	-4.4 [-7.8,-0.6]	0.989	3.0 [-1.5,7.3]	0.900
	MT+ Complex and Neighbouring Visual Areas	↑	1.6 [0.3,2.9]	0.992	↓	-6.7 [-7.7,-5.7]	1.000	↓	-1.6 [-2.8,-0.4]	0.996	-0.1 [-1.4,1.2]	0.557
	Dorsal Stream Visual Cortex	↑	1.7 [0.2,3.4]	0.986	↓	-6.6 [-7.8,-5.4]	1.000	↓	-2.7 [-4.2,-1.3]	1.000	0.4 [-1.2,2.0]	0.681
	Early Visual Cortex	↑	5.8 [3.4,8.1]	1.000	↓	-9.3 [-11.1,-7.6]	1.000	↓	-4.3 [-6.4,-2.3]	1.000	↑ 2.7 [0.5,4.9]	0.994
	Ventral Stream Visual Cortex	↑	6.3 [4.8,7.7]	1.000	↓	-7.7 [-8.8,-6.6]	1.000	↓	-3.6 [-5.0,-2.2]	1.000	1.3 [-0.2,2.8]	0.960
	Somatosensory and Motor Cortex	↑	2.1 [0.4,3.9]	0.989	↓	-5.2 [-6.5,-3.9]	1.000		-1.3 [-2.9,0.4]	0.935	-0.8 [-2.4,0.9]	0.814
	Premotor Cortex		-1.1 [-2.5,0.5]	0.916	↓	-6.0 [-7.1,-4.8]	1.000		0.1 [-1.3,1.5]	0.566	0.3 [-1.2,1.7]	0.644
	Posterior Operculum	↑	2.0 [0.4,3.5]	0.994	↓	-6.6 [-7.9,-5.4]	1.000	↓	-1.6 [-3.0,-0.3]	0.991	-0.1 [-1.7,1.5]	0.558
	Paracentral Lobular and Mid Cingulate		-0.3 [-1.6,1.1]	0.668	↓	-6.2 [-7.3,-5.2]	1.000		0.0 [-1.3,1.3]	0.508	0.4 [-0.9,1.7]	0.730
	Early Auditory Cortex	↑	2.0 [0.3,3.7]	0.989	↓	-6.4 [-7.8,-5.1]	1.000		-1.2 [-2.7,0.2]	0.950	0.8 [-0.9,2.6]	0.824
	Auditory Association Cortex	↑	5.4 [4.1,6.8]	1.000	↓	-5.0 [-6.1,-4.0]	1.000	↓	-3.2 [-4.5,-2.0]	1.000	↑ 1.9 [0.5,3.2]	0.998
	Frontal Opercular and Insular Cortex		0.0 [-1.1,1.1]	0.502	↓	-7.0 [-7.8,-6.2]	1.000	↓	-1.1 [-2.0,-0.1]	0.984	↑ 1.2 [0.1,2.3]	0.988
	Medial Temporal	↑	3.9 [2.1,5.6]	1.000	↓	-4.7 [-6.1,-3.2]	1.000	↓	-2.0 [-3.6,-0.4]	0.992	-0.3 [-2.0,1.5]	0.618
	Lateral Temporal Cortex	↑	4.6 [2.9,6.2]	1.000	↓	-4.2 [-5.5,-3.0]	1.000	↓	-2.5 [-3.9,-1.1]	0.999	0.0 [-1.6,1.7]	0.522
	Temporal-Parietal-Occipital Junction		0.7 [-0.9,2.4]	0.797	↓	-7.4 [-8.7,-6.0]	1.000		-1.0 [-2.4,0.6]	0.902	1.2 [-0.5,3.0]	0.923
	Superior Parietal and IPS	↓	-1.9 [-3.2,-0.6]	0.999	↓	-5.4 [-6.3,-4.4]	1.000		0.6 [-0.7,1.7]	0.815	0.5 [-0.8,1.7]	0.772
	Inferior Parietal Cortex		0.2 [-1.0,1.4]	0.628	↓	-6.0 [-7.0,-4.9]	1.000		-1.1 [-2.2,0.1]	0.968	-0.1 [-1.4,1.2]	0.557
	Posterior Cingulate	↑	4.1 [3.0,5.1]	1.000	↓	-5.7 [-6.5,-4.9]	1.000	↓	-1.8 [-2.8,-0.8]	1.000	-0.5 [-1.6,0.5]	0.829
	Anterior Cingulate	↑	2.6 [1.5,3.7]	1.000	↓	-5.2 [-6.1,-4.3]	1.000		-0.8 [-1.9,0.2]	0.934	↑ 1.3 [0.2,2.4]	0.988
	Orbital and Polar Frontal Cortex	↑	3.5 [2.1,4.9]	1.000	↓	-5.7 [-6.7,-4.6]	1.000		-0.2 [-1.5,1.0]	0.643	↑ 1.9 [0.6,3.3]	0.996
	Inferior Frontal Cortex	↑	1.6 [0.2,3.1]	0.989	↓	-7.4 [-8.4,-6.4]	1.000	↓	-1.4 [-2.8,-0.2]	0.987	↑ 1.9 [0.6,3.3]	0.999
	Dorsolateral Prefrontal Cortex	↑	2.2 [1.1,3.3]	1.000	↓	-5.1 [-5.9,-4.2]	1.000		-0.5 [-1.5,0.6]	0.817	1.0 [-0.1,2.1]	0.956
	Thalamus		0.9 [-0.6,2.3]	0.871	↓	-5.7 [-6.9,-4.6]	1.000		0.1 [-1.3,1.5]	0.553	0.4 [-1.1,1.9]	0.711
	Hypothalamus		0.6 [-2.1,3.5]	0.672	↓	-5.9 [-8.1,-3.7]	1.000		1.0 [-1.5,3.5]	0.774	2.6 [-0.3,5.4]	0.959
	Striatum		-1.0 [-2.5,0.4]	0.916	↓	-6.1 [-7.2,-5.0]	1.000		1.3 [-0.1,2.7]	0.968	0.7 [-0.8,2.0]	0.812
	Pallidum		-0.2 [-2.9,2.4]	0.575	↓	-6.0 [-8.1,-3.8]	1.000		0.4 [-2.0,2.7]	0.611	1.0 [-1.7,3.7]	0.762
	Basal Ganglia-Associated Nuclei		1.5 [-1.2,4.3]	0.854	↓	-6.4 [-8.6,-4.2]	1.000	↓	-3.6 [-5.9,-1.1]	0.999	0.4 [-2.5,3.4]	0.611
	Brainstem – Reticular and Sensorimotor Nuclei		-0.7 [-3.3,1.7]	0.715	↓	-5.3 [-7.5,-3.1]	1.000		0.2 [-2.3,2.4]	0.550	-0.2 [-3.0,2.7]	0.542
	Amygdala	↑	5.3 [3.0,7.7]	1.000		-0.4 [-2.4,1.5]	0.677		-1.3 [-3.3,0.7]	0.893	↓ -4.1 [-6.6,-1.6]	0.998
	Hippocampus	↑	4.8 [3.0,6.5]	1.000	↓	-2.3 [-3.6,-1.0]	0.999	↓	-2.0 [-3.5,-0.4]	0.991	↓ -2.3 [-4.1,-0.6]	0.993
	Cerebellum – Anterior Sensorimotor		-0.5 [-3.3,2.3]	0.628	↓	-4.9 [-7.0,-2.9]	1.000		1.6 [-0.9,4.2]	0.885	1.1 [-1.8,3.7]	0.757
	Cerebellum – VI (Transitional)		0.1 [-3.6,3.7]	0.521	↓	-7.0 [-9.7,-4.1]	1.000		0.4 [-3.2,4.1]	0.594	2.2 [-1.5,5.7]	0.883
	Cerebellum – Executive/Associative		0.2 [-1.7,2.1]	0.574	↓	-5.3 [-6.8,-3.8]	1.000		0.4 [-1.3,2.1]	0.701	1.8 [-0.1,3.7]	0.972
	Cerebellum – Sensorimotor VIII		-0.3 [-2.5,1.8]	0.615	↓	-3.7 [-5.5,-2.1]	1.000		1.2 [-0.8,3.2]	0.884	0.0 [-2.2,2.2]	0.511
	Cerebellum – Posterior (IX–X)		-0.6 [-2.7,1.7]	0.695	↓	-5.3 [-7.0,-3.6]	1.000	↑	2.0 [0.0,3.8]	0.976	1.7 [-0.5,4.0]	0.932
	Cerebellar Deep Nuclei	↑	4.0 [1.0,6.9]	0.996	↓	-4.3 [-6.5,-2.3]	1.000		-1.6 [-4.4,1.1]	0.876	2.0 [-0.8,4.6]	0.921

Supplementary Table 4: Microstructural inter-group comparison. Corresponding spatial maps provided in the Figure 4. Reported over larger anatomical partitions (cliques, see also Supplementary Table 1) separately for individual microstructural metrics – Neurite Density Index (NDI), Orientation Dispersion Index (ODI) and adiabatic $T_1\rho$ relaxation constant (analysed only in subcortical structures due to the field of view utilised in the MRI acquisition). Values provided as metric medians [10^{th}–90^{th} percentiles] for control and expert groups separately, followed by group differences expressed as posterior medians with 95% credible intervals (CrI) and posterior probability that the effect has the reported sign (P(sign)). Arrows indicate effects whose 95% CrI excludes zero (↑ positive, ↓ negative); effects with CrI spanning zero shown in grey. The ordering of cliques follows anatomical hierarchies across cortical, subcortical and cerebellar systems. Full numerical parcellated results are provided in the Supplementary Dataset.

	Primary Visual Cortex	0.403 [0.387,0.422]	0.404 [0.386,0.420]		-0.09 [-0.36,0.16]	0.754	0.614 [0.588,0.642]	0.629 [0.598,0.649]	↑	0.43 [0.15,0.72]	0.999				
	MT+ Complex and Neighbouring Visual Areas	0.400 [0.383,0.422]	0.406 [0.389,0.427]	↑	0.37 [0.29,0.46]	1.000	0.598 [0.556,0.647]	0.601 [0.557,0.647]		0.07 [-0.03,0.16]	0.916				
	Dorsal Stream Visual Cortex	0.398 [0.375,0.419]	0.404 [0.383,0.426]	↑	0.44 [0.33,0.55]	1.000	0.591 [0.544,0.638]	0.592 [0.550,0.633]		0.04 [-0.08,0.17]	0.738				
	Early Visual Cortex	0.407 [0.391,0.427]	0.413 [0.398,0.430]	↑	0.17 [0.01,0.33]	0.981	0.611 [0.583,0.636]	0.613 [0.590,0.637]	↑	0.17 [0.00,0.34]	0.978				
	Ventral Stream Visual Cortex	0.416 [0.392,0.437]	0.420 [0.399,0.440]	↑	0.26 [0.16,0.36]	1.000	0.603 [0.558,0.647]	0.601 [0.553,0.649]		-0.04 [-0.14,0.07]	0.746				
	Somatosensory and Motor Cortex	0.416 [0.383,0.459]	0.419 [0.388,0.454]	↑	0.22 [0.10,0.35]	1.000	0.570 [0.453,0.616]	0.575 [0.474,0.617]	↑	0.23 [0.11,0.36]	1.000				
	Premotor Cortex	0.405 [0.378,0.434]	0.409 [0.384,0.440]	↑	0.31 [0.20,0.41]	1.000	0.553 [0.506,0.596]	0.559 [0.516,0.598]	↑	0.23 [0.12,0.34]	1.000				
	Posterior Operculum	0.397 [0.377,0.419]	0.403 [0.381,0.428]	↑	0.46 [0.34,0.57]	1.000	0.569 [0.524,0.617]	0.569 [0.523,0.614]		-0.01 [-0.14,0.10]	0.591				
	Paracentral Lobular and Mid Cingulate	0.407 [0.378,0.433]	0.412 [0.383,0.440]	↑	0.33 [0.24,0.42]	1.000	0.574 [0.520,0.624]	0.578 [0.528,0.626]	↑	0.18 [0.07,0.28]	1.000				
	Early Auditory Cortex	0.424 [0.402,0.449]	0.431 [0.411,0.455]	↑	0.46 [0.34,0.58]	1.000	0.606 [0.549,0.662]	0.608 [0.560,0.662]		0.09 [-0.04,0.22]	0.909				
	Auditory Association Cortex	0.394 [0.375,0.413]	0.398 [0.379,0.416]	↑	0.32 [0.22,0.41]	1.000	0.580 [0.521,0.629]	0.579 [0.522,0.621]		-0.05 [-0.16,0.05]	0.857				
	Frontal Opercular and Insular Cortex	0.396 [0.373,0.419]	0.400 [0.377,0.423]	↑	0.37 [0.29,0.44]	1.000	0.528 [0.438,0.590]	0.535 [0.435,0.589]		0.03 [-0.06,0.11]	0.737				
	Medial Temporal	0.422 [0.399,0.468]	0.424 [0.403,0.481]	↑	0.23 [0.11,0.36]	1.000	0.576 [0.465,0.639]	0.571 [0.463,0.640]	↓	-0.13 [-0.26,0.00]	0.977				
	Lateral Temporal Cortex	0.392 [0.375,0.439]	0.397 [0.377,0.430]	↑	0.14 [0.04,0.25]	0.998	0.578 [0.530,0.622]	0.579 [0.531,0.628]		0.04 [-0.07,0.17]	0.771				
	Temporal-Parietal-Occipital Junction	0.397 [0.380,0.414]	0.404 [0.388,0.421]	↑	0.59 [0.47,0.70]	1.000	0.582 [0.543,0.622]	0.587 [0.546,0.631]	↑	0.15 [0.03,0.28]	0.991				
	Superior Parietal and IPS	0.382 [0.363,0.407]	0.390 [0.366,0.414]	↑	0.42 [0.34,0.50]	1.000	0.569 [0.514,0.616]	0.577 [0.530,0.619]	↑	0.29 [0.20,0.39]	1.000				
	Inferior Parietal Cortex	0.391 [0.373,0.409]	0.396 [0.379,0.415]	↑	0.49 [0.40,0.57]	1.000	0.572 [0.532,0.608]	0.575 [0.538,0.610]	↑	0.11 [0.02,0.20]	0.991				
	Posterior Cingulate	0.407 [0.387,0.430]	0.414 [0.394,0.436]	↑	0.55 [0.47,0.62]	1.000	0.575 [0.533,0.623]	0.573 [0.529,0.617]	↓	-0.08 [-0.16,0.00]	0.977				
	Anterior Cingulate	0.397 [0.377,0.422]	0.399 [0.378,0.425]	↑	0.19 [0.11,0.27]	1.000	0.577 [0.525,0.645]	0.573 [0.520,0.642]		-0.02 [-0.10,0.06]	0.718				
	Orbital and Polar Frontal Cortex	0.396 [0.361,0.439]	0.398 [0.366,0.432]		0.05 [-0.05,0.14]	0.832	0.591 [0.540,0.632]	0.592 [0.541,0.635]		0.05 [-0.06,0.16]	0.828				
	Inferior Frontal Cortex	0.393 [0.374,0.423]	0.398 [0.378,0.426]	↑	0.27 [0.17,0.37]	1.000	0.576 [0.531,0.618]	0.581 [0.533,0.623]	↑	0.15 [0.05,0.26]	0.998				
	Dorsolateral Prefrontal Cortex	0.390 [0.367,0.411]	0.391 [0.372,0.415]	↑	0.21 [0.14,0.28]	1.000	0.567 [0.523,0.604]	0.572 [0.529,0.611]	↑	0.22 [0.14,0.30]	1.000				
	Thalamus	0.621 [0.564,0.688]	0.624 [0.570,0.699]	↑	0.22 [0.12,0.32]	1.000	0.329 [0.279,0.389]	0.326 [0.274,0.388]		-0.08 [-0.19,0.04]	0.903	114.9 [102.8,133.0]	115.5 [105.4,133.4]		0.10 [0.00,0.19]	0.974
	Hypothalamus	0.499 [0.419,0.629]	0.504 [0.431,0.662]	↑	0.31 [0.12,0.50]	0.998	0.435 [0.352,0.525]	0.430 [0.357,0.536]		0.05 [-0.15,0.25]	0.691	156.7 [127.8,181.2]	155.5 [127.1,180.6]		0.12 [-0.06,0.29]	0.903
	Striatum	0.503 [0.469,0.549]	0.511 [0.473,0.563]	↑	0.39 [0.29,0.49]	1.000	0.607 [0.532,0.667]	0.610 [0.525,0.669]		0.10 [-0.02,0.20]	0.952	121.1 [108.4,134.9]	121.9 [109.6,137.0]	↑	0.11 [0.02,0.21]	0.990
	Pallidum	0.902 [0.790,0.979]	0.910 [0.808,0.988]		0.15 [-0.04,0.34]	0.942	0.504 [0.391,0.563]	0.514 [0.401,0.573]		0.11 [-0.10,0.32]	0.849	100.1 [90.9,111.1]	100.1 [93.8,108.8]		0.02 [-0.14,0.19]	0.601
	Basal Ganglia-Associated Nuclei	0.874 [0.753,0.946]	0.892 [0.766,0.965]		0.16 [-0.03,0.34]	0.952	0.331 [0.263,0.399]	0.331 [0.260,0.399]		0.15 [-0.06,0.35]	0.920	102.1 [87.3,115.8]	103.0 [88.9,115.3]		0.06 [-0.12,0.23]	0.731
	Brainstem – Reticular and Sensorimotor Nuclei	0.739 [0.452,0.871]	0.746 [0.458,0.879]		0.10 [-0.08,0.27]	0.868	0.343 [0.175,0.445]	0.344 [0.180,0.444]		0.15 [-0.04,0.33]	0.938	109.7 [93.6,140.5]	108.9 [96.9,140.5]		0.00 [-0.16,0.17]	0.506
	Amygdala	0.417 [0.390,0.459]	0.416 [0.390,0.465]		-0.04 [-0.19,0.12]	0.671	0.525 [0.441,0.597]	0.513 [0.431,0.578]	↓	-0.38 [-0.54,-0.21]	1.000	141.1 [127.7,159.9]	141.5 [131.4,162.9]	↑	0.17 [0.03,0.32]	0.992
	Hippocampus	0.425 [0.388,0.498]	0.421 [0.389,0.484]		-0.05 [-0.17,0.07]	0.812	0.557 [0.382,0.640]	0.551 [0.390,0.636]		-0.08 [-0.21,0.06]	0.885	130.8 [113.9,148.4]	132.3 [116.4,148.0]	↑	0.17 [0.05,0.28]	0.998
	Cerebellum – Anterior Sensorimotor	0.555 [0.507,0.607]	0.562 [0.514,0.610]	↑	0.20 [0.01,0.39]	0.982	0.518 [0.485,0.552]	0.515 [0.486,0.553]		-0.06 [-0.26,0.14]	0.737	139.5 [126.8,155.5]	137.8 [127.1,150.4]	↓	-0.19 [-0.37,-0.02]	0.984
	Cerebellum – VI (Transitional)	0.516 [0.450,0.553]	0.528 [0.468,0.562]	↑	0.34 [0.12,0.55]	0.998	0.504 [0.456,0.567]	0.501 [0.458,0.573]		0.02 [-0.22,0.26]	0.550	136.7 [125.9,151.0]	134.4 [128.0,145.2]		-0.15 [-0.35,0.06]	0.925
	Cerebellum – Executive/Associative	0.520 [0.469,0.567]	0.524 [0.482,0.565]	↑	0.14 [0.01,0.27]	0.979	0.473 [0.438,0.528]	0.466 [0.430,0.516]	↓	-0.28 [-0.42,-0.13]	1.000	137.2 [125.2,151.5]	136.2 [125.0,146.2]	↓	-0.19 [-0.31,-0.06]	0.997
	Cerebellum – Sensorimotor VIII	0.574 [0.497,0.656]	0.588 [0.510,0.658]	↑	0.35 [0.20,0.51]	1.000	0.518 [0.476,0.566]	0.509 [0.471,0.550]	↓	-0.18 [-0.35,-0.01]	0.984	142.5 [127.3,166.0]	139.3 [127.5,160.3]	↓	-0.18 [-0.32,-0.04]	0.990
	Cerebellum – Posterior (IX–X)	0.681 [0.610,0.765]	0.693 [0.608,0.768]	↑	0.19 [0.03,0.35]	0.992	0.463 [0.367,0.589]	0.462 [0.360,0.571]	↓	-0.27 [-0.44,-0.10]	1.000	147.1 [108.4,181.8]	145.9 [108.4,182.9]		-0.01 [-0.16,0.14]	0.532
	Cerebellar Deep Nuclei	0.503 [0.405,0.679]	0.518 [0.410,0.695]	↑	0.27 [0.08,0.46]	0.998	0.384 [0.301,0.557]	0.379 [0.318,0.537]		-0.03 [-0.22,0.19]	0.606	124.4 [110.4,140.9]	125.9 [110.9,141.6]		0.07 [-0.11,0.25]	0.794

Supplementary Files

This is a list of supplementary files associated with this preprint. Click to download.

- supplementarydatasetcompact.zip